

19F NMR INVESTIGATION OF CF<sub>3</sub> MOTION  
IN SOLID ZINC TRIFLUOROMETHYLSULFONATE

by

Jiankang Sun

B. Sc., East China Normal University, P. R. China, 1982

A THESIS SUBMITTED IN PARTIAL FULFILLMENT  
OF THE REQUIREMENTS FOR THE DEGREE OF  
MASTER OF SCIENCE

in the Department  
of  
Physics

ACCEPTED  
FACULTY OF GRADUATE STUDIES

We accept this dissertation as conforming  
to the required standard

DATE

April 18, 1988

DEAN

Supervisor Dr. A. Watton

Dr. G.R. Mason

Dr. P.R. West

Dr. K.R. Dixon

©JIANKANG SUN, 1987  
UNIVERSITY OF VICTORIA

All rights reserved. This dissertation may not be reproduced  
in whole or in part, by xerography or other means,  
without the permission of the author.

Supervisor: Dr. A. Watton  
moment reduction of  $5.05 \pm 0.23$  Gauss<sup>2</sup> and  
the second moment reduction from  $T_{1\rho}$  of  $4.1 \pm 0.4$  Gauss<sup>2</sup>.



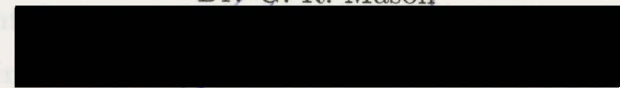
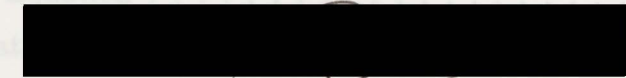
**Abstract** experiment we conclude that the  $CF_3$  lattice is rigid  
at low temperature, below 160 K, while it undergoes a rapid threshold re-  
orientation at high temperature, above 185 K.

Nuclear Magnetic Resonance studies have been made of the fluorine in Zinc Trifluoromethylsulfonate from 77 K to 296 K. Since  $I = \frac{1}{2}$  for  $^{19}F$ , we consider only the dipole-dipole interaction in the Hamiltonian. Because the local field is much smaller than the external field, the Hamiltonian is very simple in this case.

The second moment of the fluorine line shape remains essentially constant at  $7.17 \pm 0.13$  Gauss<sup>2</sup> up to about 160 K. Above this temperature it undergoes a relatively large decrease to  $2.12 \pm 0.10$  Gauss<sup>2</sup>. The relaxation time in the laboratory frame does not obey the exponential law while the relaxation time in the rotating frame does. The graphs of the relaxation times vs temperature in the laboratory and rotating frames exhibit a "V" shape as expected for thermally activated Arrhenius type molecular rotation. From the linear portions of these graphs we extract the pre-exponential factor  $\tau_0 = (2.83 \pm 0.67) \times 10^{-13}$  s and activation energy  $E_a = 21.9 \pm 0.5$  kJ/mol from  $T_1$  in the temperature range 202 K to 268 K,  $\tau_0 = (3.96 \pm 1.60) \times 10^{-13}$  s and  $E_a = 23.9 \pm 0.5$  kJ/mol from  $T_{1\rho}$  in the temperature range 194K-267 K, and  $\tau_0 = (2.38 \pm 1.13) \times 10^{-14}$  s and  $E_a = 28.4 \pm 0.6$  kJ/mol from  $T_{1\rho}$  in the temperature range 128 K to 175 K. The theoretical reduction of the second moment due to threefold re-orientation is 4.33-6.40 Gauss<sup>2</sup>, which is in reasonable agreement with the

observed experimental second moment reduction of  $5.05 \pm 0.23$  Gauss<sup>2</sup> and the second moment reduction from  $T_1(\text{min})$  of  $4.1 \pm 0.4$  Gauss<sup>2</sup>.

In the present experiment we conclude that the  $\text{CF}_3$  lattice is rigid at low temperature, below 160 K, while it undergoes a rapid threefold re-orientation at high temperature, above 185 K.

Abstract		ii
Contents		iv
Examiners:		
List of Figures		vi
List of Tables		viii
Acknowledgements	Supervisor Dr. A. Watton	ix
1 Introduction		1
	Dr. G. R. Mason	
2 Fundamentals		8
2.1 Rotational Relaxation		8
2.2 Bloch Equation	Dr. P. R. West	13
2.3 Relaxation		18
2.4 Magnetic Dipolar Broadening in Lattices	Dr. K. R. Dixon	19
2.5 Method of Moments		24
2.6 Relationship between Second Moment and Relaxation Time		27
3 Experimental Methods and Apparatus		32
3.1 Detection Methods		32
3.1.1 The Measurement of Second Moment		32
3.1.2 Measurement of $T_1$		33
3.1.3 The Measurement of $T_{1\rho}$		37

# CONTENTS

## Contents

Abstract	ii
Contents	iv
List of Figures	vi
List of Tables	viii
Acknowledgements	ix
1 Introduction	1
2 Fundamental Principles of NMR in Solids	8
2.1 Rotating Frame	8
2.2 Bloch Equation	13
2.3 Relaxation Time in the Rotating Coordinate System	18
2.4 Magnetic Dipolar Broadening of Rigid Lattices	19
2.5 Method of Moments	24
2.6 Relationship between Second Moment and Relaxation Time	27
3 Experimental Methods and Apparatus	32
3.1 Detection Methods	32
3.1.1 The Measurement of Second Moment	32
3.1.2 Measurement of $T_1$	33
3.1.3 The Measurement of $T_{1\rho}$	37

# CONTENTS

v

3.2	Experimental Apparatus . . . . .	39
3.2.1	CW Apparatus . . . . .	39
3.2.2	Pulse NMR Equipment . . . . .	43
3.2.3	DC Magnet . . . . .	46
3.2.4	The Model DTC-500 Cryogenic Temperature Controller . . . . .	49
3.3	The Zinc Triflate Sample . . . . .	49
3.4	The Measurement of Temperature . . . . .	49
4	<b>Results and Discussion</b> . . . . .	<b>50</b>
4.1	Results . . . . .	50
4.2	The Accuracy of Measurements . . . . .	54
4.3	Determination of $H_1$ . . . . .	54
4.4	Discussion . . . . .	57
4.5	Summary . . . . .	64
4.6	Suggestions . . . . .	66
	<b>References</b> . . . . .	<b>68</b>
3.1	The signal measuring $T_1$ . . . . .	35
3.2	The signal measuring $T_{1\rho}$ . . . . .	38
3.3	The block diagram of 391A Lock-in amplifier . . . . .	42
3.4	The block diagram of cw method . . . . .	44
3.5	Block diagram for coherent pulse experiment . . . . .	45
3.6	Block diagram of Model 805 Biomation Waveform Recorder . . . . .	47
3.7	The input and output of Model 805 Biomation Waveform Recorder . . . . .	48
4.1	The line shapes at 129 K (top), at 190 K (middle) and at 290 K (bottom) . . . . .	51

## List of Figures

4.2	Temperature dependence of second moment at 30 MHz . . . . .	52
4.3	A typical plot of $[(A_0 - A(\tau))/A_0]$ vs $\tau$ . . . . .	53
4.4	A typical $T_{1\rho}$ calculation graph . . . . .	55
4.5	Temperature dependence of $T_1$ and $T_{1\rho}$ . . . . .	56
4.6	$CF_3$ is tetrahedral with $C_{3v}$ symmetry in $2CF_3SO_3H \cdot H_2O$ . . . . .	60
4.7	The two extreme relative positions of two $CF_3$ groups . . . . .	61
1.1	The Larmor precession . . . . .	3
1.2	Energy levels for $I = \frac{3}{2}$ . . . . .	4
2.1	The effective magnetic field $H_{\text{eff}}$ in Eqn.(2.6) . . . . .	11
2.2	The moment precesses about the direction of $H_{\text{eff}}$ . . . . .	12
2.3	The relationship between $M_x$ and $M_{x'}$ , $M_{y'}$ . . . . .	17
2.4	Energy levels of two identical spins . . . . .	22
2.5	Absorption versus frequency . . . . .	22
2.6	Angles important in describing the rotation of a molecule . . . . .	26
2.7	$\ln T_1$ vs $1/T$ . . . . .	30
3.1	The signal measuring $T_1$ . . . . .	35
3.2	The signal measuring $T_{1\rho}$ . . . . .	38
3.3	The block diagram of 391A Lock-in amplifier . . . . .	42
3.4	The block diagram of cw method . . . . .	44
3.5	Block diagram for coherent pulse experiment . . . . .	45
3.6	Block diagram of Model 805 Biomation Waveform Recorder . . . . .	47
3.7	The input and output of Model 805 Biomation Waveform Recorder . . . . .	48
4.1	The line shapes at 129 K (top), at 190 K (middle) and at 290 K (bottom) . . . . .	51

4.2	Temperature dependence of second moment at 30 MHz . . .	52
4.3	A typical plot of $[(A_0 - A(\tau))/A_0]$ vs $\tau$ . . . . .	53
4.4	A typical $T_{1\rho}$ calculation graph. . . . .	55
4.5	Temperature dependence of $T_1$ and $T_{1\rho}$ . . . . .	56
4.6	$CF_3$ is tetrahedral with $C_{3v}$ symmetry in $2CF_3SO_3H.H_2O$ .	60
4.7	The two extreme relative positions of two $CF_3$ groups . . .	61
4.1	$t_w$ and $H_1$ for various values of $n$ . . . . .	57
4.2	The parameters of $CF_3$ groups in different compounds. . . .	59
4.3	The second moment of $^{19}F$ in motion . . . . .	60
4.4	The pre-exponential factors $\nu_0$ and activation energy $E_a$ . . .	65

# Acknowledgements

## List of Tables

I would like to express my appreciation to my supervisor Dr. A. Watton for his guidance and support throughout this work.

4.1	$t_w$ and $H_1$ for various values of $n$ . . . . .	57
4.2	The parameters of $CF_3$ groups in different compounds. . . .	59
4.3	The second moment of $^{19}F$ in motion . . . . .	60
4.4	The pre-exponential factors $\tau_0$ and activation energy $E_a$ . .	65

My assistance at the University of Victoria during September, 1985–August, 1987 is gratefully acknowledged.

# Acknowledgements

## Chapter 1

I would like to express my appreciation to my supervisor Dr. A. Watton for his guidance and support throughout this work.

I also would like to express my thanks to Mr. M. J. Rensing for his help in the experiment.

Financial support in the form of a University of Victoria Fellowship during September, 1985–August, 1987 is gratefully acknowledged.

This phenomenon was observed in bulk matter for the first time by Purcell et al. (1946) [1] and Bloch et al. (1946) [2] independently.

We will consider both quantum mechanical and classical descriptions of magnetic resonance. The classical viewpoint is particularly helpful in discussing dynamic or transient effects, while it is easy to discuss the resonance phenomenon by a simple quantum mechanical description.

A simple resonance theory is as follows [3], [4], [5].

A nucleus possesses a magnetic moment  $\mu$  and spin or intrinsic angular momentum  $J$ . In fact the two vectors may be taken as parallel so that we can write

$$\mu = \gamma J \quad (1.1)$$

where  $\gamma$  is a scalar called the "gyromagnetic ratio".

When a steady magnetic field  $H_0$  is applied to the system, the magnetic moment vector will precess about the direction of the applied field

(Figure 1.1). The equation of motion is determined by equating the torque to the rate of change of angular momentum  $\mathbf{J}$  with respect to time

$$\frac{d\mathbf{J}}{dt} = \boldsymbol{\mu} \times \mathbf{H}_0 \quad (1.2)$$

## Chapter 1

or

$$\frac{d\boldsymbol{\mu}}{dt} = \gamma \boldsymbol{\mu} \times \mathbf{H}_0 \quad (1.3)$$

## Introduction

The frequency of precession  $\omega_0$  is given by the well known Larmor precession angular frequency:

$$\omega_0 = \gamma H_0 \quad (1.4)$$

Nuclear Magnetic Resonance (NMR) is a phenomenon found in magnetic systems that possess both magnetic moments and angular momenta. This phenomenon was observed in bulk matter for the first time by Purcell et al. (1946) [1] and Bloch et al. (1946) [2] independently.

We will consider both quantum mechanical and classical descriptions of magnetic resonance. The classical viewpoint is particularly helpful in discussing dynamic or transient effects, while it is easy to discuss the resonance phenomenon by a simple quantum mechanical description.

A simple resonance theory is as follows [3], [4], [5]. In the steady field  $H_0$ , resonance occurs and energy is absorbed from the rotating field  $H_1$ .

A nucleus possesses a magnetic moment  $\boldsymbol{\mu}$  and spin or intrinsic angular momentum  $\mathbf{J}$ . In fact the two vectors may be taken as parallel so that we can write

$$\boldsymbol{\mu} = \gamma \mathbf{J} \quad (1.1)$$

where  $\gamma$  is a scalar called the "gyromagnetic ratio". The resonance phenomenon in detail by using quantum mechanics. The application of a field  $H$  produces an interaction energy of the nucleus of amount  $-\boldsymbol{\mu} \cdot \mathbf{H}$ . We have, therefore, a very simple Hamiltonian:

When a steady magnetic field  $\mathbf{H}_0$  is applied to the system, the magnetic moment vector will precess about the direction of the applied field

(Figure 1.1). The equation of motion is determined by equating the torque to the rate of change of angular momentum  $\mathbf{J}$  with respect to time

$$\frac{d\mathbf{J}}{dt} = \boldsymbol{\mu} \times \mathbf{H}_0 \quad (1.2)$$

or

$$\frac{d\boldsymbol{\mu}}{dt} = \gamma \boldsymbol{\mu} \times \mathbf{H}_0 \quad (1.3)$$

The frequency of precession  $\omega_0$  is given by the well known Larmor precession angular frequency:

$$\omega_0 = \gamma H_0 \quad (1.4)$$

If a magnetic field  $\mathbf{H}_1$ , normal to  $\mathbf{H}_0$  and rotating at some frequency  $\omega$  about  $\mathbf{H}_0$ , is applied, a torque will be exerted on  $\boldsymbol{\mu}$  causing the angle  $\theta$  between  $\mathbf{H}_0$  and  $\boldsymbol{\mu}$  to change. If  $\omega \neq \omega_0$ , or the sense of rotation of  $\mathbf{H}_1$  is opposite to that of  $\boldsymbol{\mu}$ , then the phase between  $\mathbf{H}_1$  and  $\boldsymbol{\mu}$  will be continuously changing with time and the torque will produce no net effect. If  $\mathbf{H}_1$  is made to rotate in synchronism with  $\boldsymbol{\mu}$  at the frequency  $\omega_0$ , the torque will cause the angle  $\theta$  to increase continuously. Thus when the angular frequency of  $\mathbf{H}_1$  is equal to the normal precessional frequency of the nucleus in the steady field  $\mathbf{H}_0$ , resonance occurs and energy is absorbed from the rotating field  $\mathbf{H}_1$ .

We discuss the resonance phenomenon in detail by using quantum mechanics. The application of a magnetic field  $\mathbf{H}$  produces an interaction energy of the nucleus of amount  $-\boldsymbol{\mu} \cdot \mathbf{H}$ . We have, therefore, a very simple Hamiltonian:

$$\mathcal{H} = -\boldsymbol{\mu} \cdot \mathbf{H} \quad (1.5)$$

Figure 1.1: The Larmor precession

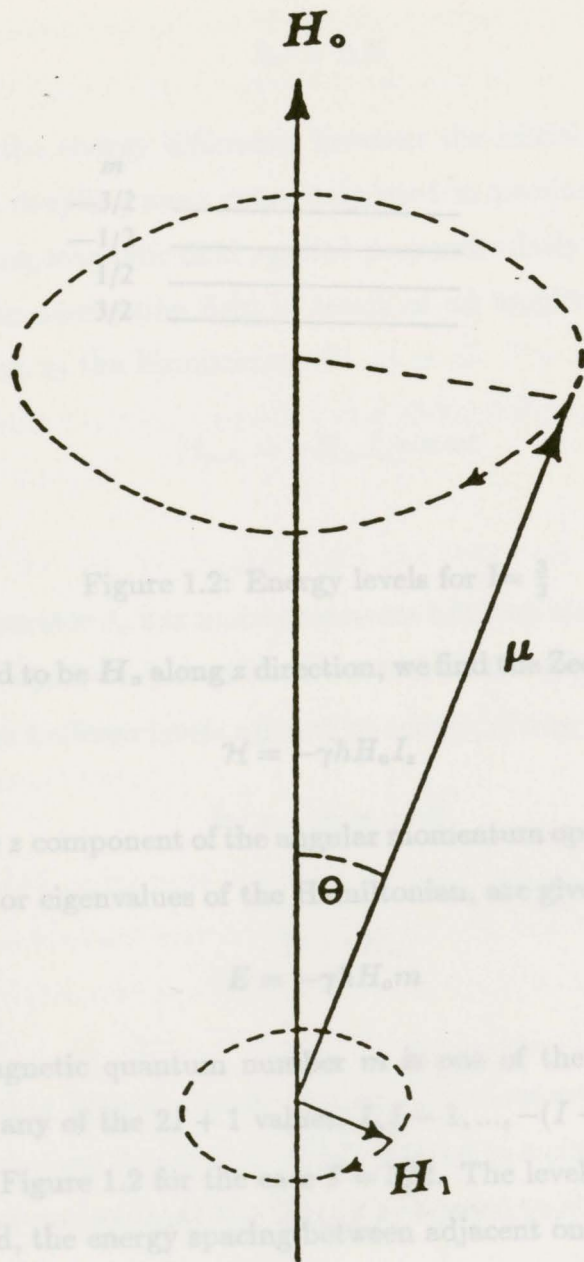


Figure 1.2: Energy levels for

Taking the field to be  $H_0$  along  $z$  direction, we find the Zeeman Hamiltonian

$$H = -\gamma \hbar H_0 I_z \quad (1.6)$$

where  $I_z$  is the  $z$  component of the angular momentum operator  $I$  ( $J = \hbar I$ ). The energies, or eigenvalues of the Hamiltonian, are given by

$$E = -\gamma \hbar H_0 m \quad (1.7)$$

where the magnetic quantum number  $m$  is one of the eigenvalues of  $I_z$  and can take any of the  $2I + 1$  values  $I, I-1, \dots, -(I-1), -I$ . They are illustrated in Figure 1.2 for the case  $I = 1/2$ . The levels in Figure 1.2 are equally spaced, the energy spacing between adjacent ones being  $\gamma \hbar H_0$ .

We hope to be able to detect the presence of such a set of energy levels by some form of spectral absorption. What is needed is to have an interaction that can cause transitions between levels. To satisfy the conservation of energy, the interaction must be time dependent and of such

Figure 1.1: The Larmor precession

an angular frequency  $\omega$  that

$$\hbar\omega = \Delta E \quad (1.8)$$

where  $\Delta E$  is the energy difference between the initial and final nuclear energies. The coupling most commonly used to produce such transitions is an alternating magnetic field, particularly to the static field. If we write the alternating field in terms of an amplitude  $H_1$ , we get a perturbing term in the Hamiltonian of

$$\mathcal{H}_{pert} = -H_1 I_x \cos \omega t \quad (1.9)$$

Figure 1.2: Energy levels for  $I = \frac{3}{2}$

Taking the field to be  $H_0$  along  $z$  direction, we find the Zeeman Hamiltonian

$$\mathcal{H} = -\gamma \hbar H_0 I_z \quad (1.6)$$

where  $I_z$  is the  $z$  component of the angular momentum operator  $I$  ( $J = \hbar I$ ).

The energies, or eigenvalues of the Hamiltonian, are given by

$$E = -\gamma \hbar H_0 m \quad (1.7)$$

where the magnetic quantum number  $m$  is one of the eigenvalues of  $I_z$ , and can take any of the  $2I + 1$  values,  $I, I - 1, \dots, -(I - 1), -I$ . They are illustrated in Figure 1.2 for the case  $I = 3/2$ . The levels in Figure 1.2 are equally spaced, the energy spacing between adjacent ones being  $\gamma \hbar H_0$ .

We hope to be able to detect the presence of such a set of energy levels by some form of spectral absorption. What is needed is to have an interaction that can cause transitions between levels. To satisfy the conservation of energy, the interaction must be time dependent and of such

an angular frequency  $\omega$  that

$$\hbar\omega = \Delta E \quad (1.8)$$

where  $\Delta E$  is the energy difference between the initial and final nuclear energies. The coupling most commonly used to produce such transitions is an alternating magnetic field applied perpendicularly to the static field. If we write the alternating field in terms of an amplitude  $H_{x0}$ , we get a perturbing term in the Hamiltonian of

$$\mathcal{H}_{pert} = -H_{x0}I_x \cos\omega t \quad (1.9)$$

The operator  $I_x$  has matrix elements between state  $m$  and state  $m'$ ,  $\langle m'|I_x|m \rangle$  which vanish unless  $m' = m \pm 1$ . Consequently, the allowed transitions are between levels adjacent in energy, giving

$$\hbar\omega = \Delta E = \gamma\hbar H_0 \quad (1.10)$$

or

$$\omega = \gamma H_0 \quad (1.11)$$

Note that Planck's constant is not in the resonance equation (1.11) which suggests that the result is closely related to a classical picture. From Eqn.(1.11) we can compute the frequency needed to observe a resonance if we know the gyromagnetic ratio  $\gamma$ .

Gorter (1936) [6] first pointed out the fact that the resonant exchange of energy between the  $2I + 1$  energy levels of a nuclear magnetic moment would occur in a magnetic field. But he unsuccessfully sought the

resonance for nuclei in crystalline lithium fluoride, and for the protons in crystalline potassium alum. Six years later Gorter and Broer (1942) [7] attempted to find the nuclear magnetic resonance absorption for  $^7\text{Li}$  in solid lithium chloride and for  $^{19}\text{F}$  in solid potassium fluoride. Again they failed. As Gorter pointed out later [8], the failure of both these attempts was mainly due to the use of unfavourable materials. The first successful cw NMR experiments using bulk materials were carried out independently at the end of 1945 by Purcell et al. and Bloch et al.. The first pulse NMR experiments followed shortly thereafter and Hahn published his famous spin echo paper in 1950 [9].

Since these breakthroughs, NMR has been used as a tool in the investigation of a variety of topics, e.g., the determination of nuclear magnetic moments, the identification of nuclei present in a given substance, the determination of chemical shifts, and the study of micro dynamical behaviour of molecules in matter.

The NMR absorption spectrum provides information concerning the structure of molecules and crystals (Gutowsky, Kistiakowsky, Pake and Purcell, 1949) [10], and molecular motion in crystals (Gutowsky and Pake, 1950) [11]. Purcell [12] has emphasized the importance of additional information which may be obtained from measurements of the spin-lattice relaxation time. Materials containing fluorine groups such as  $\text{AsF}_5^{2-}$  [13],  $\text{CF}_3$  [14],  $\text{SbF}_5^{2-}$  [15],  $\text{TiF}_6^{2-}$  [16],  $\text{SiF}_6^{2-}$  [17] and  $\text{CHF}_3$  [18] have been studied. But materials, containing the trifluoromethylsulfonate (triflate) ion ( $\text{CF}_3\text{SO}_3^-$ ) have seldom been studied.

This thesis deals with the study of zinc triflate by measurement of

the second moment, relaxation time  $T_1$  and relaxation time in the rotating frame  $T_{1\rho}$ . Therefore, we shall give the fundamental theory concerning second moment and relaxation time in Chapter 2. In Chapter 3 the experimental apparatus and the experimental technique are described. The experimental results are presented and discussed in Chapter 4.

## Fundamental Principles of NMR in Solids

### 2.1 Rotating Frame

It is very helpful to discuss the motion of the magnetization not only in the fixed coordinate system of the laboratory, as we did in Chapter 1, but also in a coordinate system that rotates about  $H_0$  in the same direction in which the nuclear moments precess. This coordinate system is often called the rotating frame of reference or, commonly, the rotating frame [3], [5].

The effect of an alternating magnetic field  $H_1(t) = H_1 \cos \omega t$ , which has been mentioned in Chapter 1, is most readily analyzed by breaking it into two rotating components, each of amplitude  $H_1/2$ , one rotating clockwise and the other counterclockwise. We denote these rotating fields by  $H_R$  and  $H_L$ .

$$\begin{aligned} H_R &= H_1/2 (\cos \omega t + j \sin \omega t) \\ H_L &= H_1/2 (\cos \omega t - j \sin \omega t) \end{aligned} \quad (2.1)$$

Since one component will rotate in the same sense as the precession of the moments and the other in the opposite sense, the counter rotating compo-

nents may be neglected near the resonance. We shall assume we have only the field  $H_R$ , but this is no loss in generality because the use of a negative  $\omega$  will convert it to  $H_L$ . In order to reserve the symbol  $\omega$  for a positive quantity, we shall introduce the symbol  $\omega_1$ , which is the component of  $\omega$  along the direction of  $H_0$ .  $\omega_1$  may therefore be positive or negative.<sup>1</sup>

## Chapter 2

# Fundamental Principles of NMR in Solids

## 2.1 Rotating Frame

It is very helpful to discuss the motion of the magnetization not only in the fixed coordinate system of the laboratory, as we did in Chapter 1, but also in a coordinate system that rotates about  $H_0$  in the same direction in which the nuclear moments precess. This coordinate system is often called the rotating frame of reference or, commonly, the rotating frame [3], [5].

The effect of an alternating magnetic field  $H_x(t) = H_{x0} \cos \omega t$ , which has been mentioned in Chapter 1, is most readily analyzed by breaking it into two rotating components, each of amplitude  $H_1$ , one rotating clockwise and the other counterclockwise. We denote these rotating fields by  $H_R$  and  $H_L$ .

$$\begin{aligned} H_R &= H_1(i \cos \omega t + j \sin \omega t) \\ H_L &= H_1(i \cos \omega t - j \sin \omega t) \end{aligned} \quad (2.1)$$

Since one component will rotate in the same sense as the precession of the moments and the other in the opposite sense, the counter rotating compo-

nents may be neglected near the resonance. We shall assume we have only the field  $\mathbf{H}_R$ , but this is no loss in generality because the use of a negative  $\omega$  will convert it to  $\mathbf{H}_L$ . In order to reserve the symbol  $\omega$  for a positive quantity, we shall introduce the symbol  $\omega_z$ , which is the component of  $\omega$  along the  $z$ -axis.  $\omega_z$  may therefore be positive or negative.<sup>1</sup>

We write

$$\mathbf{H}_1 = H_1(\mathbf{i} \cos \omega_z t + \mathbf{j} \sin \omega_z t) \quad (2.2)$$

which will give us either sense of rotation, depending on the sign of  $\omega_z$ .

The equation of motion of a spin including the effects both of  $\mathbf{H}_1(t)$  and of the static field  $\mathbf{H}_0 = kH_0$  is

$$\frac{d\boldsymbol{\mu}}{dt} = \boldsymbol{\mu} \times \gamma[\mathbf{H}_0 + \mathbf{H}_1(t)] \quad (2.3)$$

We can eliminate the time dependence of  $\mathbf{H}_1$  by using a coordinate system that rotates about the  $z$  direction at frequency  $\omega_z$ . In such a coordinate system,  $\mathbf{H}_1$  will be static. Since the axis of rotation coincides with the direction of  $\mathbf{H}_0$ ,  $\mathbf{H}_0$  will also be static. Let the  $x$ -axis be in the rotating frame along  $\mathbf{H}_1$ . Then Eqn.(2.3) becomes

$$\frac{d\boldsymbol{\mu}}{dt} = \boldsymbol{\mu} \times [k(\omega_z + \gamma H_0) + \mathbf{i}\gamma H_1] \quad (2.4)$$

Here we have encountered two effects in making the transformation of Eqn. (2.3) to Eqn.(2.4). The first is associated with the derivative of the rotating unit vectors and gives the term  $\omega_z$ . The second is associated with expressing the vectors  $\mathbf{H}_0$  and  $\mathbf{H}_1$  in terms of their components in the rotating system and gives rise to the conversion of  $\mathbf{H}_1$  from a rotating to a static field.

<sup>1</sup>See Reference [5] Chapter 2.

Eqn.(2.4) may be rewritten to emphasize that near resonance  $\omega_z + \gamma H_0 \simeq 0$ , by setting  $\omega_z = -\omega$ , where  $\omega$  is now positive (We assume here that  $\gamma$  is positive). Then

$$\begin{aligned} \frac{d\boldsymbol{\mu}}{dt} &= \boldsymbol{\mu} \times \gamma \left[ \left( H_0 - \frac{\omega}{\gamma} \right) \mathbf{k} + H_1 \mathbf{i} \right] \\ &= \gamma \boldsymbol{\mu} \times \mathbf{H}_{eff} \end{aligned} \quad (2.5)$$

where

$$\mathbf{H}_{eff} = \mathbf{k} \left( H_0 - \frac{\omega}{\gamma} \right) + \mathbf{i} H_1 \quad (2.6)$$

Eqn.(2.5) states that in the rotating frame, the moment acts as though it experiences effectively a static magnetic field  $\mathbf{H}_{eff}$  (Figure 2.1). The moment therefore precesses in a cone of fixed angle about the direction of  $\mathbf{H}_{eff}$  at angular frequency  $\gamma H_{eff}$ . The situation is illustrated in Figure 2.2 for a magnetic moment which, at  $t = 0$ , was oriented along the  $z$ - direction. Let  $\mathbf{M}$  be the vector sum of the  $\boldsymbol{\mu}$ 's, then by summing Eqn.(2.5) vectorially over all  $\boldsymbol{\mu}$  we obtain the following relation for the macroscopic magnetization:

$$\frac{d\mathbf{M}}{dt} = \gamma \mathbf{M} \times \mathbf{H}_{eff}$$

Figure 2.1: The effective magnetic field  $\mathbf{H}_{eff}$  in Eqn.(2.6)

After the field  $\mathbf{H}_1$  is turned off, the magnetization will precess freely about  $\mathbf{H}_0$ . In an actual experiment, the precessing magnetization decays owing to various mechanisms which usually are the objects of an NMR study. In a coil with its axis perpendicular to the laboratory field, this decaying magnetization will induce an rf current at the Larmor frequency, in complete

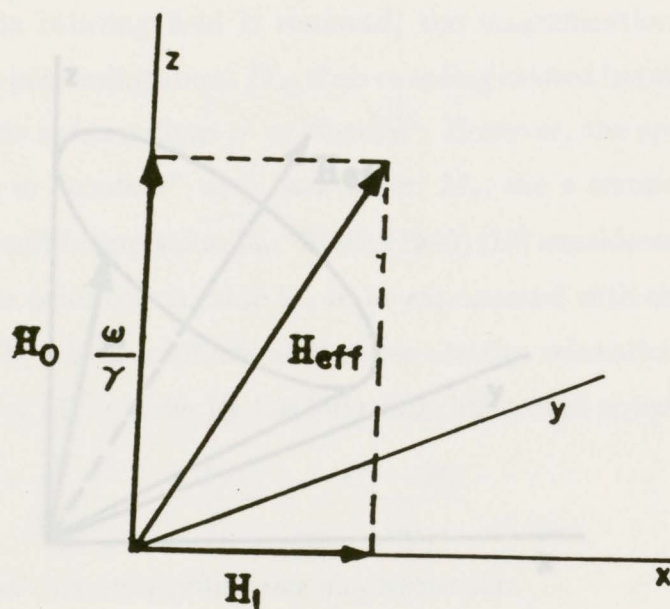
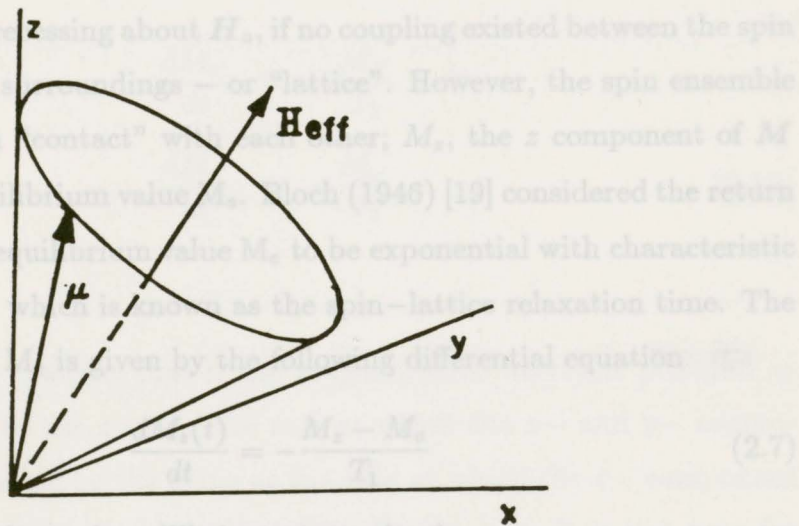


Figure 2.1: The effective magnetic field  $H_{\text{eff}}$  in Eqn.(2.6)

analogy with an electrical generator. The signal induced in the coil is free precession signal and, owing to its decay, is called the free induction decay (FID).

## 2.2 Bloch Equation

After the rotating field is removed, the magnetization vector  $M$  would continue precessing about  $H_0$ , if no coupling existed between the spin ensemble and its surroundings - or "lattice". However, the spin ensemble and lattice are in "contact" with each other;  $M_z$ , the  $z$  component of  $M$  will attain its equilibrium value  $M_0$ . Bloch (1946) [19] considered the return of  $M_z$  toward its equilibrium value  $M_0$  to be exponential with characteristic time constant  $T_1$ , which is known as the spin-lattice relaxation time. The rate of change of  $M_z$  is given by the following differential equation:



$$\frac{dM_z}{dt} = -\frac{M_z - M_0}{T_1} \quad (2.7)$$

where  $M_0$  is the thermal equilibrium magnetization.

We combine (2.7) with the equation for the driving of  $M$  by the torque to get

$$\frac{dM_z}{dt} = -\frac{M_z - M_0}{T_1} + \gamma(M \times H_0)_z \quad (2.8)$$

Figure 2.2: The moment precesses about the direction of  $H_{\text{eff}}$

Furthermore we wish to express the fact that in thermal equilibrium under a static field, the magnetisation will be parallel to  $H_0$ . That is, the  $x$ - and  $y$ - components must have a tendency to vanish. Thus

$$\frac{dM_x}{dt} = \gamma(M \times H_0)_x = \frac{M_y}{T_2}$$

analogy with an electrical generator. The signal induced in the coil is a free precession signal and, owing to its decay, is called the free induction decay (FID).

## 2.2 Bloch Equation

After the rotating field is removed, the magnetization vector  $M$  would continue precessing about  $H_0$ , if no coupling existed between the spin ensemble and its surroundings — or “lattice”. However, the spin ensemble and lattice are in “contact” with each other;  $M_z$ , the  $z$  component of  $M$  will attain its equilibrium value  $M_0$ . Bloch (1946) [19] considered the return of  $M_z$  toward its equilibrium value  $M_0$  to be exponential with characteristic time constant  $T_1$  which is known as the spin–lattice relaxation time. The rate of change of  $M_z$  is given by the following differential equation

$$\frac{dM_z(t)}{dt} = -\frac{M_z - M_0}{T_1} \quad (2.7)$$

where  $M_0$  is the thermal equilibrium magnetization.

We combine (2.7) with the equation for the driving of  $M$  by the torque to get

$$\frac{dM_z(t)}{dt} = -\frac{M_z - M_0}{T_1} + \gamma(\mathbf{M} \times \mathbf{H}_0)_z \quad (2.8)$$

Furthermore we wish to express the fact that in thermal equilibrium under a static field, the magnetization will be parallel to  $H_0$ . That is, the  $x$ - and  $y$ - components must have a tendency to vanish. Thus

$$\frac{dM_x}{dt} = \gamma(\mathbf{M} \times \mathbf{H}_0)_x - \frac{M_x}{T_2}$$

$$\frac{dM_y}{dt} = \gamma(\mathbf{M} \times \mathbf{H}_0)_y - \frac{M_y}{T_2} \quad (2.9)$$

Here we have introduced the relaxation time constant  $T_2$  for the  $x$ - and  $y$ -components, which we call spin-spin relaxation time. Since the effective field is zero in the rotating frame, Eqn.(2.9) can be simplified by transformation into a frame rotating about the  $z$ -axis with angular frequency  $\omega_0$ ,

$$\begin{aligned} \frac{dM_{x'}}{dt} &= -\frac{M_{x'}}{T_2} \\ \frac{dM_{y'}}{dt} &= -\frac{M_{y'}}{T_2} \end{aligned} \quad (2.10)$$

It may be thought that if the magnetization vector is pictured as slowly tilting up to the  $z$ -axis, the rate at which the  $x$ - and  $y$ - components decrease should be the same as the rate at which the  $z$ - component increases. While this would be true for a single spin, it is not true for the magnetization vector representing an ensemble of mutually interacting spins in a normal inhomogeneous field. All the  $z$ -components of the individual spin vectors will add in the  $z$ -direction to give a resultant  $M_z$ . However, due to the local fields and field inhomogeneities, the components of individual spins in the  $x$ - $y$  plane will precess at slightly different rates, and get out of phase with each other. Thus the vector sums in the  $x'$  and  $y'$  directions will shrink quickly. It might be expected, therefore, that  $T_2 < T_1$ . This is the typical situation for solids.

If a rotating field of amplitude  $H_1$  and angular frequency  $\omega$  is applied in the  $x - y$  plane in addition to  $\mathbf{H}_0$ , the total field in the laboratory frame

is

$$\mathbf{H} = iH_1 \cos \omega t + jH_1 \sin \omega t + kH_0 \quad (2.11)$$

Transforming to a frame rotating about the  $z$ -axis with this angular frequency  $\omega$  gives the effective field

The above result  $\mathbf{H}_{eff} = i'H_1 + k'(H_0 + \frac{\omega}{\gamma})$  (2.12) or expressed in terms of equivalent angular precession frequencies  $\omega_0 = -\gamma H_0$  and  $\omega_1 = -\gamma H_1$

$$\mathbf{H}_{eff} = \frac{1}{\gamma} [k'(\omega - \omega_0) - i'\omega_1] \quad (2.13)$$

Equations (2.13) show that the magnetization is a constant in the rotating reference frame, and therefore is rotating at frequency  $\omega$  in the laboratory frame. In a typical experiment, we observe the magnetization by studying the emf induced in a fixed coil in the laboratory frame.

If the coil is oriented along the  $x$ -axis. From the time-dependence of magnetization  $M_x$  along the  $x$ -axis. From the laboratory component  $M_x$  and the  $x', y'$ -components in the rotating frame is

$$\begin{aligned} \frac{dM_{x'}}{dt} &= M_{y'}(\omega - \omega_0) - \frac{M_{x'}}{T_2} \\ \frac{dM_{y'}}{dt} &= -M_{z'}\omega_1 - M_{x'}(\omega - \omega_0) - \frac{M_{y'}}{T_2} \\ \frac{dM_{z'}}{dt} &= M_{y'}\omega_1 + \frac{M_0 - M_{z'}}{T_1} \end{aligned} \quad (2.14)$$

These are the Bloch equations in the rotating frame.

A steady state solution can easily be found if the time derivatives of the three components are zero. (2.17) we have

$$M_{x'} = \frac{\gamma H_1 T_2^2 (\omega - \omega_0)}{1 + T_2^2 (\omega - \omega_0)^2 + \gamma^2 H_1^2 T_1 T_2} M_0$$

$$\begin{aligned}
 M_{y'} &= \frac{\gamma H_1 T_2}{1 + T_2^2(\omega - \omega_0)^2 + \gamma^2 H_1^2 T_1 T_2} M_0 \\
 M_{z'} &= \frac{1 + T_2^2(\omega - \omega_0)^2}{1 + T_2^2(\omega - \omega_0)^2 + \gamma^2 H_1^2 T_1 T_2} M_0
 \end{aligned} \tag{2.15}$$

The above results contain in the denominator the quantity  $1 + \gamma^2 H_1^2 T_1 T_2$ . In the non-saturated weak-field case,  $\gamma^2 H_1^2 T_1 T_2 \ll 1$ , we have

$$\begin{aligned}
 M_{x'} &= \frac{\gamma H_1 T_2^2 (\omega - \omega_0)}{1 + T_2^2(\omega - \omega_0)^2} M_0 \\
 M_{y'} &= \frac{\gamma H_1 T_2}{1 + T_2^2(\omega - \omega_0)^2} M_0
 \end{aligned} \tag{2.16}$$

Equations (2.15) show that the magnetization is a constant in the rotating reference frame, and therefore is rotating at frequency  $\omega$  in the laboratory frame. In a typical experiment, we observe the magnetization by studying the emf induced in a fixed coil in the laboratory frame.

If the coil is along the  $x$ -direction in the laboratory, we can calculate the emf from the time-dependence of magnetization  $M_x$  along the  $x$ -axis. From Figure 2.3 the relationship between the laboratory component  $M_x$  and the  $x'$ -,  $y'$ - components in the rotating frame is

$$M_x = M_{x'} \cos \omega t + M_{y'} \sin \omega t \tag{2.17}$$

The voltage induced in the coil along the  $x$  direction will be proportional to  $\frac{dM_x}{dt}$ , and from Eqn.(2.17) we have

$$\frac{dM_x}{dt} = \omega(-M_{x'} \sin \omega t + M_{y'} \cos \omega t)$$

## 2.3 Relaxation Time in the Rotating Coordinate System

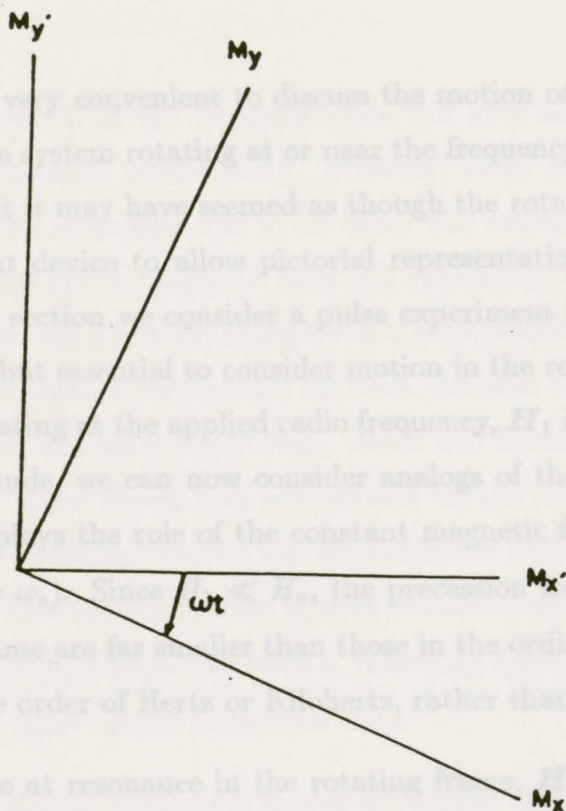


Figure 2.3: The relationship between  $M_x$  and  $M_{x'}$ ,  $M_y$ ,

## 2.3 Relaxation Time in the Rotating Coordinate System

It is very convenient to discuss the motion of the magnetization in a coordinate system rotating at or near the frequency of the applied rf. Up to this point it may have seemed as though the rotating frame was merely a convenient device to allow pictorial representation of the behaviour of  $M$ . In this section we consider a pulse experiment in which it is not only convenient but essential to consider motion in the rotating frame. Since in a frame rotating at the applied radio frequency,  $H_1$  is constant in direction and magnitude, we can now consider analogs of the pulse experiment, in which  $H_1$  plays the role of the constant magnetic field  $H_0$  when at resonance ( $\omega = \omega_0$ ). Since  $H_1 \ll H_0$ , the precession frequencies found in the rotating frame are far smaller than those in the ordinary laboratory frame, i.e., in the order of Hertz or Kilohertz, rather than Megahertz.

Since at resonance in the rotating frame,  $H_1$  plays the role of the fixed field, the relaxation of  $M$  in the direction of  $H_1$  is analogous in some ways to spin-lattice relaxation. For this reason the relaxation is characterized by a time  $T_{1\rho}$ , usually called the spin-lattice relaxation time in the rotating frame, and the signal decays with this time constant.

Clearly  $T_{1\rho}$  must be closely related to  $T_2$ , for in the absence of  $H_1$ , relaxation along the  $x'$  axis is characterized by  $T_2$ . In fact, for most liquids,  $T_{1\rho} = T_2$ . But in solids,  $T_{1\rho}$  is usually quite different from  $T_2$ , and the study of  $T_{1\rho}$  can provide information on molecular reorientation processes that cannot be obtained from ordinary  $T_1$  and  $T_2$  measurements alone.

<sup>2</sup>See Reference [5] Chapter 3.

## 2.4 Magnetic Dipolar Broadening of Rigid Lattices

The width of the resonance line will give some useful information about the material under study. However, there are a number of effects that cause the resonance line to be wide. For example, the inhomogeneity of the applied static magnetic field will contribute to the line width. If a nucleus possesses a nonvanishing electric quadrupole moment, the degeneracy of the resonance frequencies between different  $m$  values may be lifted, giving rise to unresolved splittings, which will broaden the resonance. We shall ignore these effects and concentrate on the contribution of the magnetic dipole coupling between the various nuclei to the width of the Zeeman transition. This approximation is often excellent, particularly when the nuclei have spin  $1/2$  (and therefore a vanishing quadrupole moment) and a rather long spin-lattice relaxation time.<sup>2</sup>

The classic interaction energy  $E$  between two magnetic moments,  $\mu_1$  and  $\mu_2$ , is

$$E = \frac{\mu_1 \cdot \mu_2}{r^3} - \frac{3(\mu_1 \cdot \mathbf{r})(\mu_2 \cdot \mathbf{r})}{r^5} \quad (2.18)$$

where  $\mathbf{r}$  is the radius vector from  $\mu_1$  to  $\mu_2$ . Therefore the general dipolar contribution to the Hamiltonian for  $N$  spins is

$$\mathcal{H}_d = \frac{1}{2} \sum_{j=1}^N \sum_{k=1}^N \left[ \frac{\mu_j \cdot \mu_k}{r_{jk}^3} - \frac{3(\mu_j \cdot \mathbf{r}_{jk})(\mu_k \cdot \mathbf{r}_{jk})}{r_{jk}^5} \right] \quad (2.19)$$

where  $\mathbf{r}_{jk}$  is the radius vector from  $\mu_j$  to  $\mu_k$  and the factor  $1/2$  is introduced because the sums over  $j$  and  $k$  would count each pair twice. Since  $\mu = \gamma \hbar \mathbf{I}$

<sup>2</sup>See Reference [5] Chapter 3.

( $\mathbf{I}$  is the spin operator), by writing  $\boldsymbol{\mu}_1$  and  $\boldsymbol{\mu}_2$  in component form and omitting the subscripts from  $\mathbf{r}$  we see from Eqn.(2.18) that the dipolar Hamiltonian will contain terms such as

$$D = -\frac{\gamma_1\gamma_2\hbar^2}{r^3} I_{1x}I_{2x}$$

$$E = -\frac{\gamma_1\gamma_2\hbar^2}{r^5} I_{1x}I_{2x} \frac{xy}{r^2}$$

where we assume that both the gyromagnetic ratios and spins may be different. If we express  $I_x$  and  $I_y$  in terms of the raising and lowering operator  $I^+$  and  $I^-$ :

$$I_x = \frac{1}{2}(I^+ + I^-)$$

$$I_y = \frac{1}{2i}(I^+ - I^-)$$

and express the rectangular coordinates  $x, y, z$  in terms of spherical coordinates  $r, \theta, \phi$ :

$$r = \sqrt{x^2 + y^2 + z^2}$$

$$\tan\phi = \frac{y}{x}$$

$$\tan\theta = \frac{\sqrt{x^2 + y^2}}{z} \quad (2.21)$$

we may write the Hamiltonian in a form that is particularly convenient for computing matrix elements:

$$\mathcal{H}_d = \frac{\gamma_1\gamma_2}{r^3}(A + B + C + D + E + F) \quad (2.20)$$

where

$$A = I_{1z}I_{2z}(1 - 3\cos^2\theta)$$

$$B = -\frac{1}{4}(I_1^+ I_2^- + I_1^- I_2^+)(1 - 3\cos^2\theta)$$

$$C = -\frac{3}{2}(I_1^+ I_{2z} + I_{1z} I_2^+) \sin\theta \cos\theta e^{-i\phi}$$

$$D = -\frac{3}{2}(I_1^- I_{2z} + I_{1z} I_2^-) \sin\theta \cos\theta e^{i\phi}$$

$$E = -\frac{3}{4} I_1^+ I_2^+ \sin^2\theta e^{-2i\phi}$$

$$F = -\frac{3}{4} I_1^- I_2^- \sin^2\theta e^{2i\phi}$$

We can estimate that  $\mu/r^3 \sim 1$  Gauss. Therefore the term  $\gamma_1\gamma_2\hbar^2/r^3$  corresponds to the interaction of a nuclear moment with a local field of about 1 Gauss, whereas the Zeeman Hamiltonian  $\mathcal{H}_Z = -\gamma_1\hbar H_0 I_{1z} - \gamma_2\hbar H_0 I_{2z}$  corresponds to an interaction with a field of  $\sim 10^4$  Gauss. Therefore we can solve the Zeeman problem first and then treat the dipolar term as a perturbation.

We consider a simple example of two identical moments of spin  $\frac{1}{2}$  to see the significance of the various term A, B, C, D, E and F. The Zeeman energy in this case is

$$E_z = -\gamma\hbar H_0 m_1 - \gamma\hbar H_0 m_2 \quad (2.21)$$

where  $m_1$  and  $m_2$  are the eigenvalues of the operator  $I_{1z}$  and  $I_{2z}$  respectively.

The Zeeman energy level scheme is shown in Figure 2.4. It is convenient to denote a state in which  $m_1 = +\frac{1}{2}, m_2 = -\frac{1}{2}$  by the notation  $|+-\rangle$ . In the Figure 2.4, the two states  $|+-\rangle$  and  $|-+\rangle$  are degenerate in zeroth order, and both have  $E_z = 0$ . The states  $|++\rangle$  and  $|--\rangle$  have  $E_z = -\hbar\omega_0$  and  $+\hbar\omega_0$  respectively, where  $\omega_0 = \gamma H_0$ .



to the zero-order function  $u_n^o$  of zero-order energy  $E_n$ :

$$u_n = u_n^o + \sum_{n'} \frac{\langle n' | \mathcal{H}_{pert} | n \rangle}{E_n - E_{n'}} u_{n'}^o \quad (2.22)$$

where  $u_n$  is the wave function corrected for the effect of the perturbation  $\mathcal{H}_{pert}$  and the matrix elements  $\langle n' | \mathcal{H}_{pert} | n \rangle$  are computed between the unperturbed states of  $u_{n'}^o$  and  $u_n^o$ . The term  $\langle n' | \mathcal{H}_{pert} | n \rangle$  will be  $\gamma^2 \hbar^2 / r^3$  multiplied by a spin matrix element, which is always of order unity. Therefore  $\langle n' | \mathcal{H}_{pert} | n \rangle \sim \gamma^2 \hbar^2 / r^3 \simeq \gamma \hbar H_{loc}$  while  $E_n - E_{n'} = \hbar \omega_o = \gamma \hbar H_o$ , so that

$$\left| \frac{\langle n' | \mathcal{H}_{pert} | n \rangle}{E_n - E_{n'}} \right| \approx \frac{H_{loc}}{H_o} \sim 10^{-4}$$

corresponding to a very small admixture. Therefore the intensity of absorption is much weaker by the ratio of  $(H_{loc}/H_o)^2$ . These transitions occur at  $\omega = 2\omega_o$  and  $\omega = 0$  as shown in Figure 2.5. The extra peaks are very weak and may therefore be dropped. The remaining dipolar term  $A + B$  is

$$\mathcal{H}_d^o = \frac{\gamma^2 \hbar^2}{2r^3} (1 - 3\cos^2\theta) (3I_{1z}I_{2z} - \mathbf{I}_1 \cdot \mathbf{I}_2) \quad (2.23)$$

The total simplified Hamiltonian becomes

$$\mathcal{H} = \sum_k (-\gamma \hbar H_o I_{zk}) + \frac{1}{4} \gamma^2 \hbar^2 \sum_{j,k} \frac{1 - 3\cos^2\theta_{jk}}{r_{jk}^3} (3I_{jz}I_{kz} - \mathbf{I}_j \cdot \mathbf{I}_k) \quad (2.24)$$

It is difficult to find the eigenfunctions in the general case. But we can use the so-called method of moments, a clever technique due to Van Vleck [20], to compute properties of the resonance line without solving explicitly for the eigenstates and eigenvalues of energy.

## 2.5 Method of Moments

The  $n$ th moment is defined by the equation

$$\langle \omega^n \rangle = \frac{\int_0^\infty \omega^n f(\omega) d\omega}{\int_0^\infty f(\omega) d\omega} \quad (2.25)$$

or

$$\langle \Delta\omega^n \rangle = \frac{\int_0^\infty (\omega - \langle \omega \rangle)^n f(\omega) d\omega}{\int_0^\infty f(\omega) d\omega} \quad (2.26)$$

where  $f(\omega)$  is the line shape function.

The expression for  $n = 2$  is called the “second moment”, which Van Vleck calculated for like nuclei to be

$$\langle \Delta\omega^2 \rangle = \frac{3}{4} \gamma^4 \hbar^2 I(I+1) \frac{1}{N} \sum_{j,k} \frac{(1 - 3\cos^2\theta_{jk})^2}{r_{jk}^6} \quad (2.27)$$

where  $r_{jk}$  is the distance between nuclei  $j$  and  $k$ , and  $\theta_{jk}$  is the angle between  $\mathbf{r}_{jk}$  and the direction of the external magnetic field. We can get a clear understanding of Eqn.(2.27) by considering an example in which all spins are located in equivalent positions, so that

$$\sum_k \frac{(1 - 3\cos^2\theta_{jk})^2}{r_{jk}^6}$$

is independent of  $j$ .

There are  $N$  equivalent sums, one for each value of  $j$ , giving us

$$\langle \Delta\omega^2 \rangle = \frac{3}{4} \gamma^4 \hbar^2 I(I+1) \sum_k \frac{(1 - 3\cos^2\theta_{jk})^2}{r_{jk}^6} \quad (2.28)$$

For a powder made of crystallites of random orientation it is permissible to average  $(1 - 3\cos^2\theta_{jk})^2$  over all directions, leading to [3]

$$\langle (\Delta\omega^2) \rangle = \frac{3}{5}\gamma^4\hbar^2 I(I+1) \sum_k \frac{1}{r_{jk}^6} \quad (2.29)$$

An important property of the second moment is its dependence on temperature resulting from the molecular motion. The effect of rotation may be expressed very simply in terms of the angles defined in Figure 2.6. We consider a pair of nuclei  $j, k$  fixed in a molecule, the axis of rotation of the molecule making an angle  $\theta'$  with respect to the static field  $\mathbf{H}_0$ . Let the radius vector from  $j$  to  $k$  make an angle  $\gamma_{jk}$  with the rotation axis. As the molecule rotates, the angle  $\theta_{jk}$  varies with time. If the frequency of rotation is high compared with the frequencies of interest in the resonance, it is the time average of  $1 - 3\cos^2\theta_{jk}$  that affects the second moment. Assuming the motion is over a potential well of threefold or higher symmetry, this average can be shown to be independent of the details of the motion as

$$\langle 1 - 3\cos^2\theta_{jk} \rangle_{avg} = (1 - 3\cos^2\theta') \frac{3\cos^2\gamma_{jk} - 1}{2} \quad (2.30)$$

In a powder sample we find all orientations of the crystal axes with respect to  $\mathbf{H}_0$ . For a rigid lattice we must average  $(1 - 3\cos^2\theta_{jk})^2$  over the random crystal orientations. When motion sets in we first average  $1 - 3\cos^2\theta_{jk}$  over the motion to obtain the second moment for a given crystal orientation. Then we must average over crystal orientation.

For interacting pairs, the contribution to the second moment of the

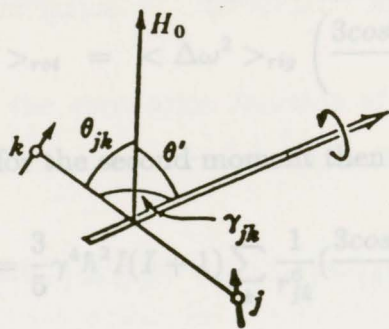


Figure 2.6: Angles important in describing the rotation of a molecule

rigid lattice  $\langle \Delta\omega^2 \rangle_{rig}$  then goes as

$$\langle \Delta\omega^2 \rangle_{rig} \propto \overline{(1 - 3\cos^2\theta_{jk})^2} \tag{2.31}$$

where the bar indicates an average over the random orientations of  $\theta_{jk}$ .

When rotation sets in, we have a second moment from the pair  $\langle \Delta\omega^2 \rangle_{rot}$  given by

$$\langle \Delta\omega^2 \rangle_{rot} \propto \overline{(\langle 1 - 3\cos^2\theta_{jk} \rangle_{avg})^2} \tag{2.32}$$

where the ‘‘avg’’ indicates an average over rotation, and the bar indicates an average of the orientation of the rotation axis with respect to  $H_0$ . By using Eqn.(2.30) we get

$$\langle \Delta\omega^2 \rangle_{rot} \propto \overline{(1 - 3\cos^2\theta')^2} \left( \frac{3\cos^2\gamma_{jk} - 1}{2} \right)^2 \tag{2.33}$$

Since the crystal axes and the rotation axes are randomly oriented with

respect to  $\mathbf{H}_0$ ,

$$\overline{(1 - 3\cos^2\theta_{jk})^2} = \overline{(1 - 3\cos^2\theta')^2}$$

$$\langle \Delta\omega^2 \rangle_{rot} = \langle \Delta\omega^2 \rangle_{rig} \left( \frac{3\cos^2\gamma_{jk} - 1}{2} \right)^2 \quad (2.37)$$

The expression for the second moment then is and by

$$(\Delta\omega^2)_{rot} = \frac{3}{5}\gamma^4\hbar^2 I(I+1) \sum_k \frac{1}{r_{jk}^6} \left( \frac{3\cos^2\gamma_{jk} - 1}{2} \right)^2 \quad (2.34)$$

where  $\gamma_{jk}$  is the angle between the radius vector  $\mathbf{r}_{jk}$  and the rotation axis.

Eqn.(2.29) and Eqn.(2.34) are very important in discussing the molecular motion.

## 2.6 Relationship between Second Moment and Relaxation Time.

According to the weak collision theory developed by Bloembergen, Purcell and Pound (BPP theory) [21] and subsequently revised and generalized by others [22], [23], [24], the relaxation times along the static magnetic field  $\mathbf{H}_0$  and rotating magnetic field  $\mathbf{H}_1$  for a pair of nuclei separated by a distance  $r$  have been shown to be

$$T_1^{-1} = \frac{3}{2}\gamma^4\hbar^2 I(I+1)[J^{(1)}(\omega_0) + J^{(2)}(2\omega_0)], \quad (2.35)$$

and

$$T_{1\rho}^{-1} = \frac{3}{2}\gamma^4\hbar^2 I(I+1)\left[\frac{1}{4}J^{(0)}(2\omega_1) + \frac{5}{2}J^{(1)}(\omega_0) + \frac{1}{4}J^{(2)}(2\omega_0)\right], \quad (2.36)$$

where  $J^{(q)}(\omega)$  are the spectral densities of the fluctuating dipolar interaction  $J^q(\omega)$  given by

$$J^{(q)}(\omega) = \int_{-\infty}^{+\infty} G^{(q)}(\tau) e^{-i\omega\tau} d\tau \quad (2.37)$$

where  $G^{(q)}(t)$  is called the correlation function of the Hamiltonian  $\mathcal{H}(t)$ .  $G^q(t)$  tells how  $\mathcal{H}(t)$  at one time is correlated to its value at a later time, and by

$$G^{(q)}(\tau) = \langle F^{(-q)}(t + \tau) F^{(q)}(t) \rangle \quad (2.38)$$

where the brackets  $\langle \rangle$  denoting an ensemble average and  $F^{(q)}$  is the geometrical factor for the interaction Eqn.(2.20) given by

$$\begin{aligned} F^{(0)}(t) &= (1 - 3 \cos^2 \theta) r^{-3}, \\ F^{(1)}(t) &= \sin \theta \cos \theta e^{-i\phi} r^{-3}, \\ F^{(2)}(t) &= \sin^2 \theta e^{-2i\phi} r^{-3}. \end{aligned} \quad (2.39)$$

For times less than some critical time  $\tau_c$ , called "the correlation time", the motion may be considered negligible, so that

$$F^{(q)}(t) \simeq F^{(q)}(t + \tau)$$

For  $\tau > \tau_c$ , the value of  $F^{(q)}(t + \tau)$  becomes progressively less correlated with  $F^{(q)}(t)$  as  $\tau$  is lengthened, so that  $G(\tau)$  goes to zero. Thus  $G(\tau)$  has a maximum at  $\tau = 0$ , and falls off for  $|\tau| > \tau_c$ .

It has been shown [25] that for an exponential  $G(\tau)$  the typical term in Eqn.(2.37) looks like  $\tau_c / (1 + \omega^2 \tau_c^2)$ . Then Eqn.(2.35) and Eqn(2.36) can

be written as

$$\frac{1}{T_1} = \frac{2}{3} \gamma^2 \Delta M_2 \left( \frac{\tau_c}{1 + \omega_o^2 \tau_c^2} + \frac{4\tau_c}{1 + 4\omega_o^2 \tau_c^2} \right) \quad (2.40)$$

and

$$\frac{1}{T_{1\rho}} = \frac{\gamma^2 \Delta M_2}{3} \left( \frac{3\tau_c}{1 + 4\omega_1^2 \tau_c^2} + \frac{5\tau_c}{1 + \omega_o^2 \tau_c^2} + \frac{2\tau_c}{1 + 4\omega_o^2 \tau_c^2} \right) \quad (2.41)$$

where  $\omega_o$  is the nuclear precession frequency,  $H_1 = \omega_1/\gamma$  is the rotating field strength,  $\tau_c$  is the correlation time for the motion and  $\Delta M_2$  is the reduction of the second moment for the same motion<sup>3</sup>. For thermally activated processes,  $\tau_c$  is usually taken to have a temperature dependence given by the Arrhenius expression

$$\tau_c = \tau_o \exp(E_a/kT) \quad (2.42)$$

where  $k$  is the Boltzmann constant and  $E_a$  the activation energy for molecular reorientation. There are many experimental studies which bear out the validity of this assumption.

From Eqn.(2.40) and (2.42), the variation of  $\ln T_1$  with  $1/T$  will consist of a 'V' shaped curve. It is easy to prove that the minimum occurs at  $\omega_o \tau = 0.6158$  as shown in Figure 2.7. The curve is dependent on the spectrometer frequency, lower frequencies shifting the minimum to lower temperature. The two curves differ at low temperatures but are identical at high temperatures. On the low temperature side,  $\omega_o^2 \tau_c^2 \gg 1$ , and from Eqn.(2.40) and Eqn.(2.42) we have

$$T_1 \propto e^{E_a/kT}$$

<sup>3</sup>Hereafter the symbol  $M_2$  refers to the second moment expressed in Gauss<sup>2</sup>.

A plot of  $\ln T_1$  vs  $T^{-1}$  will give a line of slope  $E_a/k$ , leading to a value for the activation energy  $E_a$ , governing the principal motion occurring over that range of temperature. Similarly, at high temperatures  $\omega_c^2 \tau_c^2 \ll 1$ , Eqn.(2.40) and Eqn.(2.42) reduce to

$$T_1 \propto e^{-E_a/kT}$$

$E_a$  again being found from the slope of a plot of  $\ln T_1$  vs  $T^{-1}$ . The determination of the activation energies governing the motion from  $T_1$  measurements is an important aspect of solid state NMR. The activation energy  $E_a$  may also be found from the limiting slopes of  $\ln T_1$  vs  $T^{-1}$  in the high and low temperature region.

The motion responsible for the relaxation will also produce a second moment reduction  $\Delta M_2$  when the associated correlation time becomes less than the inverse linewidth. The second moment reduction is related to the coupling constant for the same motion by

$$\Delta M_2 = \frac{1.05\omega_c}{\gamma^2 T_1(\text{ms})} \quad (2.43)$$

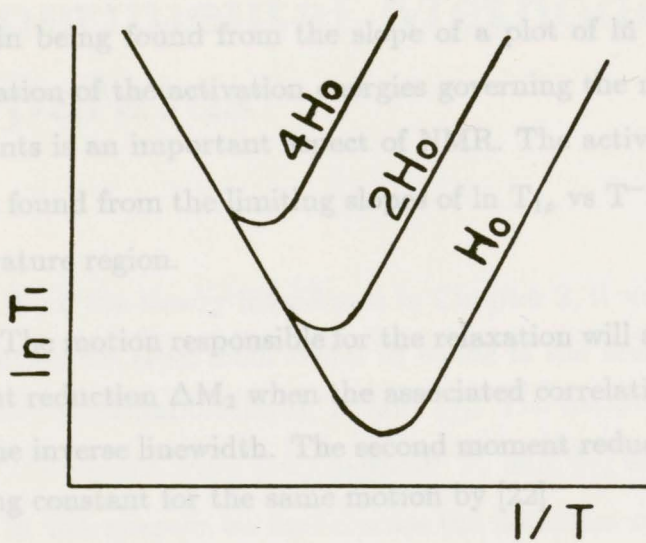


Figure 2.7:  $\ln T_1$  vs  $1/T$

A plot of  $\ln T_1$  vs  $T^{-1}$  will give a line of slope  $E_a/k$ , leading to a value for the activation energy  $E_a$ , governing the principal motion occurring over that range of temperature. Similarly, at high temperatures  $\omega_0^2\tau_c^2 \ll 1$ , Eqn.(2.40) and Eqn.(2.42) reduce to

$$T_1 \propto e^{-E_a/kT}$$

$E_a$  again being found from the slope of a plot of  $\ln T_1$  vs  $T^{-1}$ . The determination of the activation energies governing the motion from  $T_1$  measurements is an important aspect of NMR. The activation energy  $E_a$  may also be found from the limiting slopes of  $\ln T_{1\rho}$  vs  $T^{-1}$  in the high and low temperature region.

The motion responsible for the relaxation will also produce a second moment reduction  $\Delta M_2$  when the associated correlation time becomes less than the inverse linewidth. The second moment reduction is related to the coupling constant for the same motion by [22]

$$\Delta M_2 = \frac{1.05\omega_0}{\gamma^2 T_{1(min)}} \tag{2.43}$$

### 3.1 Detection Methods

#### 3.1.1 The Measurement of Second Moment

The definition of second moment is

$$\langle \Delta \omega^2 \rangle = \frac{\int_{-\infty}^{\infty} (\omega - \langle \omega \rangle)^2 f(\omega) d\omega}{\int_{-\infty}^{\infty} f(\omega) d\omega} \tag{3.1}$$

Since the signal we detect is the derivative line, we express (3.1) in terms of the derivative line shape written as

$$\langle \Delta\omega^2 \rangle = \frac{\int_0^\infty (\omega - \langle \omega \rangle)^2 g(\omega) d\omega}{\int_0^\infty (\omega - \langle \omega \rangle) g(\omega) d\omega} \quad (3.2)$$

where  $g(\omega) = f'(\omega)$ , is the derivative line shape function.

## Chapter 3 Experimental Methods and Apparatus

$$\langle \Delta\omega^2 \rangle = \frac{\sum_{n=0}^N (\omega(n) - \langle \omega \rangle)^2 g(n)}{3 \sum_{n=0}^N (\omega(n) - \langle \omega \rangle) g(n)} \quad (3.3)$$

From the theory introduced in Chapter 2, it was seen that the basic information we need from NMR in solids is the second moment  $M_2$  and spin-lattice relaxation times,  $T_1$  and  $T_{1\rho}$ . The second moment is measured by the continuous wave (cw) method;  $T_1$  and  $T_{1\rho}$  are measured by pulse NMR. In this chapter we first discuss the detection methods [3], [25], then the experimental apparatus.

### 3.1 Detection Methods

#### 3.1.1 The Measurement of Second Moment

The definition of second moment is

$$\langle \Delta\omega^2 \rangle = \frac{\int_0^\infty (\omega - \langle \omega \rangle)^2 f(\omega) d\omega}{\int_0^\infty f(\omega) d\omega} \quad (3.1)$$

An ensemble of nuclear spins (the sample) is placed inside a coil having its axis along the  $x$ -direction of a cartesian coordinate system.

<sup>1</sup>The program was written by M.J. Reading.

Since the signal we detect is the derivative line, we express (3.1) in terms of the derivative line shape written as

$$\langle \Delta\omega^2 \rangle = \frac{\int_0^\infty (\omega - \langle \omega \rangle)^3 g(\omega) d\omega}{3 \int_0^\infty (\omega - \langle \omega \rangle) g(\omega) d\omega} \quad (3.2)$$

where  $g(\omega) = f'(\omega)$ , is the derivative line shape function.

Therefore the second moment is calculated by numerical integration of the line shape

$$\langle \Delta\omega^2 \rangle = \frac{\sum_{n=0}^N [\omega(n) - \langle \omega \rangle]^3 g(n)}{3 \sum_{n=0}^N [\omega(n) - \langle \omega \rangle] g(n)} \quad (3.3)$$

This is done by the computer. The program consists of three parts. The first one inputs the experimental conditions such as temperature, sweep range and sweep time and a number of cw scans, and stores them with the sampled data sequentially, via a 12 bit A/D convertor, in a temporary data file. The second part finds the baseline, using the least squares method, and the average line shape and average second moment. The third part displays the lineshape and prints the result<sup>1</sup>. The work is done on an IBM PC-XT.

### 3.1.2 Measurement of $T_1$

The spin-lattice relaxation time measurements were made using the pulse method of Hahn (1950) [9]. The method is briefly discussed below.

An ensemble of nuclear spins (the sample) is placed inside a coil having its axis along the  $x$ -direction of a cartesian coordinate system.

<sup>1</sup>The program was written by M.J.Rensing.

The coil is placed in a constant magnetic field  $\mathbf{H}_0$  applied along the  $z$  direction. When the spins have reached thermal equilibrium a macroscopic magnetic moment  $\mathbf{M} = \mathbf{M}_0$  is set up parallel to  $\mathbf{H}_0$ . An rf pulse of Larmor frequency  $\omega_0$  is now applied to the coil so that the spin ensemble is subjected to a linearly polarized rf field,  $H_x = 2H_1 \cos \omega_0 t$ , where  $|H_1| \ll |H_0|$ .  $H_x$  can be considered to be made up of two circularly polarized fields as in Eqn.(2.1) rotating in the  $x$ - $y$  plane in opposite senses with  $\omega = \omega_0$ . As we mentioned in section (2-1), we consider only one of them, which is in phase with the precession of  $\mathbf{M}$  and tips the magnetic moment vector away from the direction of  $\mathbf{H}_0$  by an angle

$$\theta = \gamma H_1 t_w \quad (3.4)$$

where  $t_w$  is the duration of the rf pulse.

The magnetic moment vector  $\mathbf{M}$ , precessing about  $\mathbf{H}_0$  at an angle  $\theta$ , will have a component in the  $x - y$  plane rotating about  $\mathbf{H}_0$  and as a result an rf voltage is induced in the same coil used for the generation of the rf field. This induced voltage will be maximum when the magnetic moment vector  $\mathbf{M}$  is in the  $x$ - $y$  plane, i.e., when  $\theta = \pi/2$ . The induced voltage decays due to damping effects such as spin-lattice relaxation, spin-spin relaxation, an inhomogeneous dc field, etc. Thus a decaying signal, called free induction decay or FID, is observed following the rf pulse.

If a second pulse is applied at a time  $\tau$  after the first pulse, a free induction decay is also observed after the second pulse. The maximum amplitude of this free induction signal depends upon the regrowth of the  $z$ -component of the magnetization during  $\tau$ . The signal observed following a pair of equal pulses applied to a spin ensemble initially in thermal equilibrium are shown in Figure 3.1.  $A_0$  and  $A(\tau)$  are the maximum FID

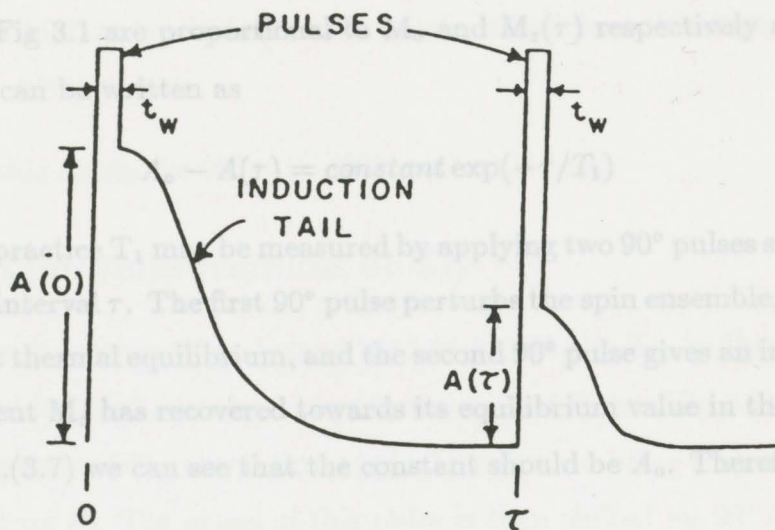


Figure 3.1: The signal measuring  $T_1$

amplitudes following the first and second pulse respectively.

If a pulse of width  $t_w$  is applied to a spin ensemble at time  $t = 0$ , then immediately following the pulse  $t = t_w$  and  $M_z$  (z-component of  $M$ ) is equal to  $M_z(t_w)$ . Solving Eqn.(2.7) using these initial conditions leads to

$$M_z(t) - M_0 = [M_z(t_w) - M_0] \exp[-(t - t_w)/T_1] \quad (3.5)$$

If a second pulse of width  $t_w$  is applied at  $t = \tau$  and  $t_w \ll \tau$ , Eqn.(3.5) becomes

$$M_0 - M_z(\tau) = \text{constant} \exp(-\tau/T_1) \quad (3.6)$$

Similar to  $T_1$ ,  $T_2$ , the magnitude of  $M_z$  will not change appreciably during the time  $t_w$ . The signal amplitude immediately following the pulse

can then be considered proportional to the value of  $M_z$  at the beginning of the pulse. This means that the maximum FID amplitudes  $A_0$  and  $A(\tau)$  shown in Fig 3.1 are proportional to  $M_0$  and  $M_z(\tau)$  respectively and thus Eqn.(3.6) can be written as

$$A_0 - A(\tau) = \text{constant} \exp(-\tau/T_1) \quad (3.7)$$

In practice  $T_1$  may be measured by applying two  $90^\circ$  pulses separated by a time interval  $\tau$ . The first  $90^\circ$  pulse perturbs the spin ensemble, which is initially at thermal equilibrium, and the second  $90^\circ$  pulse gives an indication of the extent  $M_z$  has recovered towards its equilibrium value in the time  $\tau$ . From Eqn.(3.7) we can see that the constant should be  $A_0$ . Therefore (3.7) is

$$A_0 - A(\tau) = A_0 \exp(-\tau/T_1) \quad (3.8)$$

The sequence of two  $90^\circ$  pulses is repeated for different values of  $\tau$  at a repetition frequency that allows enough time between successive sequences for the spin ensemble to reach thermal equilibrium. Measuring the amplitude  $A(\tau)$  as a function of  $\tau$ ,  $T_1$  is found from a slope of  $\ln[A_0 - A(\tau)] - \ln A_0$  against  $\tau$ .

The  $90^\circ - \tau - 90^\circ$  sequence is called a recovery sequence. There is another type of sequence to measure  $T_1$ ,  $180^\circ - \tau - 90^\circ$ , which is called an inversion recovery sequence. The first pulse inverts the magnetization and the recovery therefore goes from  $-M_0$  to  $M_0$ . Integration of equation (2.7) with the initial condition  $M_z = -M_0$  at  $t = 0$  gives

$$M_z(\tau) = M_0[1 - 2\exp(-\tau/T_1)] \quad (3.9)$$

Similarly, we can get from Eqn.(3.9) the equation

$$\ln(A_0 - A(\tau)) = \ln 2A_0 - \tau/T_1 \quad (3.10)$$

where  $A(\tau)$  is the initial amplitude of the FID following the  $90^\circ$  pulse at time  $\tau$ , and  $A_0$  is the limiting value of  $A(\tau)$  for a very long interval between the  $180^\circ$  and  $90^\circ$  pulse. Therefore  $T_1$  is determined from the slope of a plot of  $\ln(A_0 - A(\tau))$  vs  $\tau$ .

In this thesis the  $90^\circ - \tau - 90^\circ$  method is used.

### 3.1.3 The Measurement of $T_{1\rho}$

The experimental technique used to obtain the  $T_{1\rho}$  in this thesis is called "spin locking", developed by Hartmann and Hahn (Fig 3.2) [9], [46]. An on-resonance  $90^\circ$  pulse is first applied along  $x'$  to bring the magnetization  $M_0$  along  $y'$ . The phase of this pulse is then shifted by  $90^\circ$  so that it is now applied along  $y'$ , that is, in the same direction as the magnetization vector. This second pulse is called the "spin locking" pulse and while it is being applied, the spins are said to be "spin-locked". In the absence of this second pulse there would be simple decay of the  $y'$  magnetization due to  $T_2$  relaxation processes. The spin-locking pulse acts as a static field and is applied for a time  $\tau$ , during which there will be some decay of the  $y'$  magnetization obeying the law

$$M(t) = M_0 e^{-t/T_{1\rho}} \quad (3.11)$$

which may be detected by recording the FID immediately after the locking pulse. From the variation of signal intensity with  $\tau$ ,  $T_{1\rho}$  can be found from the slope of  $\ln M(\tau)$  against  $\tau$  or  $\ln A(\tau)$  against  $\tau$ .

### 3.2 Experimental Apparatus

Cw and Pulsed NMR spectrometers are quite similar in some respects. They both require a transmitter for generating the  $H_1$  rf field, a preamplifier-receiver-detector unit for processing the nuclear signal, and sample circuitry to contain the sample and to couple the sample to both the transmitter and receiver. The pulse widths for these various units are quite different. The pulse widths for the transmitter may be Kilowatts at the sample, while the receiver usually operates in the range 10-400 Gauss since an NMR signal is very weak. The receiver must be able to withstand large overvoltages and recover very quickly (10  $\mu$ sec or faster) from overload; this problem rarely if ever arises in cw NMR work. In pulsed NMR the sample circuitry must be able to handle large rf voltages (100-1000 V) of a very short duration (about 10  $\mu$ sec), but it must also be able to process the weak nuclear signal in such a way that a high sensitivity is achieved; in cw NMR only very low rf fields are used and the sample circuitry can be designed for maximum sensitivity, therefore the circuitry for cw NMR work is rather straight forward [43].

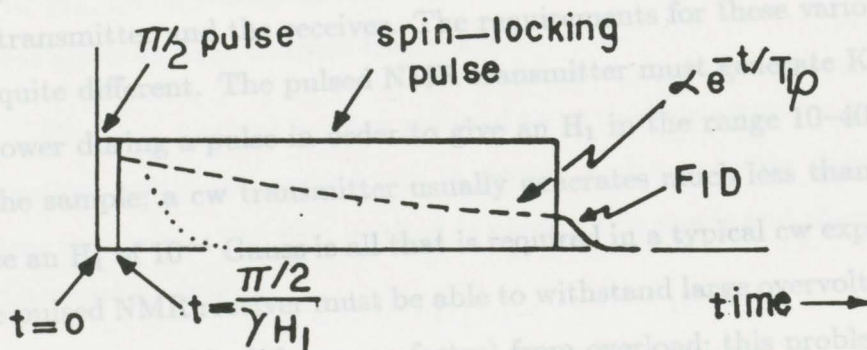


Figure 3.2: The signal measuring  $T_{1\rho}$  in this thesis. In this thesis, the spin-locking pulse is used to measure  $T_{1\rho}$  in cw and pulsed NMR experiments in this thesis.

#### 3.2.1 CW Apparatus

The methods for detecting the cw signal can be broadly split into two categories:

## 3.2 Experimental Apparatus

Cw and Pulsed NMR spectrometers are quite similar in some respects. They both require a transmitter for generating the  $H_1$  rf field, a preamplifier–receiver–detector unit for processing the nuclear signal, and sample circuitry to contain the sample and to couple the sample to both the transmitter and the receiver. The requirements for these various units are quite different. The pulsed NMR transmitter must generate Kilowatts of power during a pulse in order to give an  $H_1$  in the range 10–400 Gauss at the sample; a cw transmitter usually generates much less than 1 Watt since an  $H_1$  of  $10^{-4}$  Gauss is all that is required in a typical cw experiment. The pulsed NMR receiver must be able to withstand large overvoltages and recover very quickly (10  $\mu$ sec or faster) from overload; this problem rarely if ever arises in cw NMR work. In pulsed NMR the sample circuitry must be able to handle large rf voltages (100–1000 V) of a very short duration (about 10  $\mu$ sec), but it must also be able to process the weak nuclear signal in such a way that a high sensitivity is achieved; in cw NMR only very low rf fields are used and the sample circuitry can be designed for maximum sensitivity, therefore the circuitry for cw NMR work is rather straight forward [43].

In this chapter we discuss the equipment relevant to the cw and pulsed NMR experiments in this thesis.

### 3.2.1 CW Apparatus

The methods for detecting the cw signal can be broadly split into two categories:

1) A single coil method in which the change in susceptibility of the sample when resonance occurs changes the effective inductance of a coil which surrounds the sample and is part of a tuned circuit.

2) A double coil method in which one coil is fed from a signal generator and the second coil, mutually orthogonal to the transmitter coil axis and to  $H_0$ , has a voltage induced in it due to the forced precession of the nuclear spins at their Larmor frequency.

The first method is often referred to as nuclear magnetic resonance absorption, while the second one is simply and accurately described as nuclear induction. The first method is used in this thesis and therefore will be discussed in detail.

### Detector

The marginal oscillator CW spectrometer used in this experiment was supplied by Spin-Lock Electronics. The equipment is tuned for a particular frequency. In this experiment it is 30 MHz, so we can sweep the magnetic field over quite a large range in order to find the resonance point.

mixer and, via the phase shifter, to the phase sensitive detector.

In this experiment the EXT mode was used. The reference input was generated by Wavetek 114.

Particular attention was given to the lock-in amplifier.

### Modulation

Additional audiofrequency modulation is used by superimposing a small sinusoidal field variation. The carrier is modulated by an amount whose amplitude and phase carry information about the slope of the ab-

### Dynatrac 391A Lock-in Amplifier

A lock-in amplifier is used to amplify the weak signals of known frequency and phase. The input signal is amplified and passed through a 24 db/octave low pass filter set just above the highest frequency for that range. The amplified signal is mixed with a signal  $f_v$ , thus translating any coherent input (i. e., at the reference frequency  $f_r$ ) to the constant IF frequency  $f_o$ . This signal goes through a differential amplifier to the band pass amplifier centered at  $f_o$ , which removes harmonically related signals and further restricts the band width, thus eliminating interference that would overload conventional lock-ins.  $f_o$  is set at about 25 times the maximum operating frequency. The phase sensitive detector and the output amplifier perform similar functions in conventional instruments. The block diagram of 391A Lock-in amplifier is shown in Figure 3.3.

In the EXT mode, the phase lock loop, consisting of the phase detector, voltage controlled oscillator (VCO) and reference mixer, phase-lock the reference mixer output to the external reference signal. A fixed frequency sine oscillator generates  $f_o$ , which is an input to both the reference mixer and, via the phase shifter, to the phase sensitive detector.

In this experiment the EXT mode was used. The reference input was generated by Wavetek 114.

Figure 3.3: The block diagram of 391A Lock-in amplifier

### Modulation

Additional audiofrequency modulation is used by superimposing a small sinusoidal field variation. The carrier is modulated by an amount whose amplitude and phase carry information about the slope of the ab-

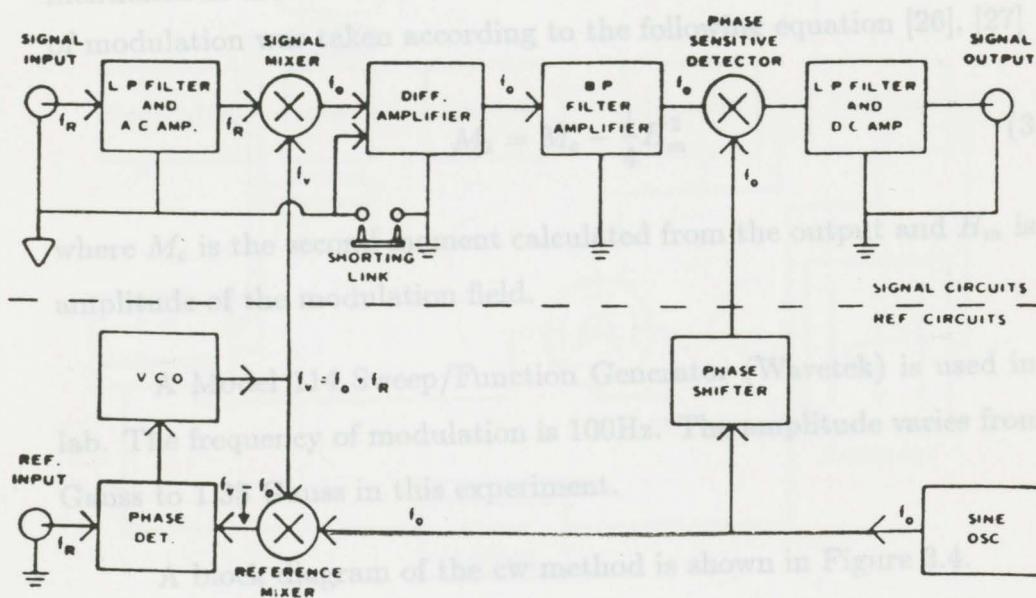


Figure 3.3: The block diagram of 391A Lock-in amplifier

### 3.2.2 Pulse NMR Equipment

#### Coherent NMR Pulse Spectrometer-CPS2

A train of pulses occurring at times  $t_1, t_2, \dots, t_k$  and of duration  $\tau_1, \tau_2, \dots, \tau_k$  can be represented by the function

$$H(t) = \sum A_k(t) \cos(\omega t + \phi_k) \quad (3.13)$$

where  $A_k(t) = 0$  outside of the interval  $t_k \leq t \leq t_k + \tau_k$  and is approximately constant inside. The pulses are called incoherent if the phases are

sorption signal at any point. In this experiment we display the absorption signal on an X-Y chart recorder to make sure that the signal is not saturated or distorted by too large a modulation or too high a level of the marginal oscillator. Then the output is sampled and converted to input data for a suitable computer program to determine the second moment as mentioned in the section 3.1.3. A correction to the moments for the effects of modulation was taken according to the following equation [26], [27]

$$M_2 = M_c - \frac{1}{4}H_m^2 \quad (3.12)$$

where  $M_c$  is the second moment calculated from the output and  $H_m$  is the amplitude of the modulation field.

A Model 114 Sweep/Function Generator (Wavetek) is used in the lab. The frequency of modulation is 100Hz. The amplitude varies from 0.7 Gauss to 1.35 Gauss in this experiment.

A block diagram of the cw method is shown in Figure 3.4.

### 3.2.2 Pulse NMR Equipment

#### Coherent NMR Pulse Spectrometer—CPS2

The oscillating rf field produced in a coil by a sequence of pulses occurring at times  $t_1, t_2, \dots, t_k$  and of duration  $\tau_1, \tau_2, \dots, \tau_k$  can be represented by the function

$$H(t) = \sum_k A_k(t) \cos(\omega t + \varphi_k) \quad (3.13)$$

where  $A_k(t) = 0$  outside of the interval  $t_k \leq t \leq t_k + \tau_k$  and is approximately constant inside. The pulses are called incoherent if the phases are

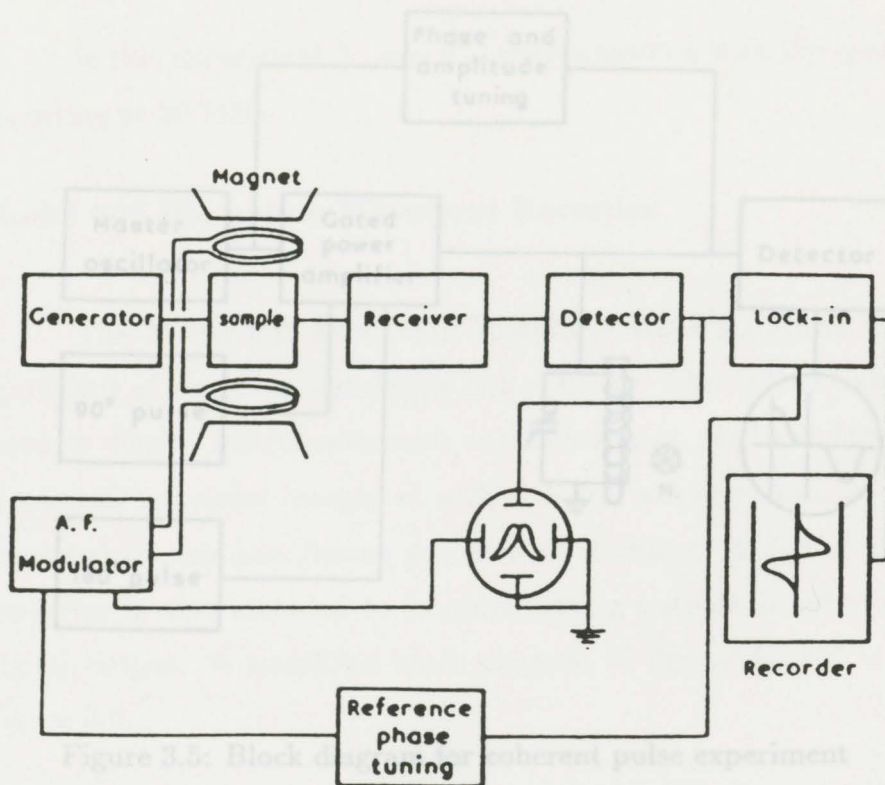


Figure 3.5: Block diagram of coherent pulse experiment

distributed at random, and coherent if their values can be controlled (in particular, given the same value  $\varphi$ ). The coherent pulse method was used in this experiment and a block diagram of the experimental set up is shown in Figure 3.5.

Figure 3.4: The block diagram of cw method

In this method a master oscillator that generates the radio-frequency runs continuously. The power amplifier is gated to connect or disconnect at prescribed intervals, or "gate", the power amplifier that produces the large rf  $H_1$ . CPS2 also has a preamplifier-receiver-detector unit for processing the nuclear signal, and sample circuitry to couple the sample to both the transmitter and the receiver. CPS2 can generate single pulse, two pulse, spin-locking and CPMG (Carr-Purcell and Gill-Meiboom) sequences.

The time period is five decades from 0.1 msec to 10 sec with equally spaced settings in each of the five decades.

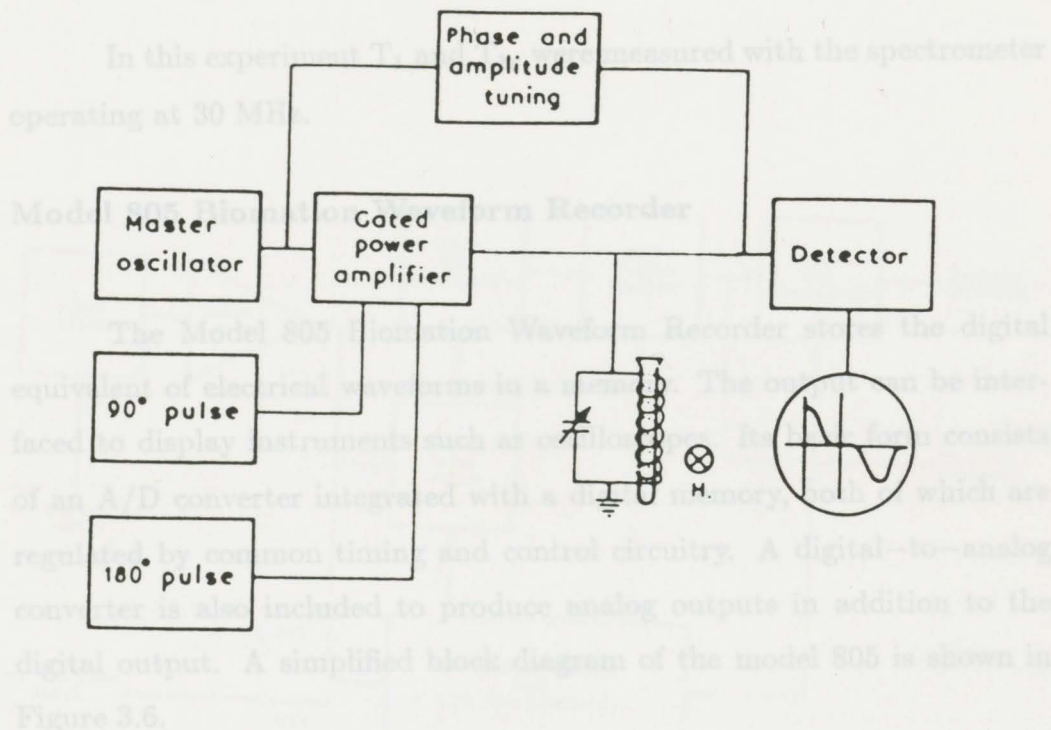


Figure 3.5: Block diagram for coherent pulse experiment

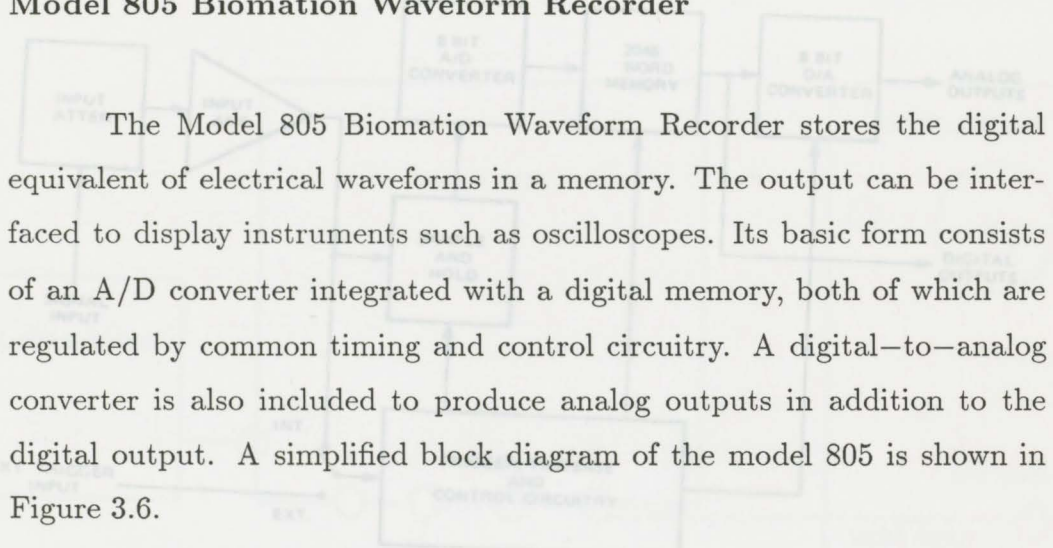
The signal and trigger inputs of model 805 are connected to the distributed at random, and coherent if their values can be controlled (in particular, given the same value  $\varphi$ ). The coherent pulse method was used in this experiment and a block diagram of the experimental set up is shown in Figure 3.5.

In this method a master oscillator that generates the radio-frequency runs continuously and the role of the timer is to connect or disconnect at prescribed intervals, or "gate", the power amplifier that produces the large rf  $H_1$ . CPS2 also has a preamplifier-receiver-detector unit for processing the nuclear signal, and sample circuitry to couple the sample to both the transmitter and the receiver. CPS2 can generate single pulse, two pulse, spin-locking and CPMG (Carr-Purcell and Gill-Meiboom) sequences.

The time period is five decades from 0.1 msec to 10 sec with equally spaced settings in each of the five decades.

In this experiment  $T_1$  and  $T_{1\rho}$  were measured with the spectrometer operating at 30 MHz.

### Model 805 Biomation Waveform Recorder



The Model 805 Biomation Waveform Recorder stores the digital equivalent of electrical waveforms in a memory. The output can be interfaced to display instruments such as oscilloscopes. Its basic form consists of an A/D converter integrated with a digital memory, both of which are regulated by common timing and control circuitry. A digital-to-analog converter is also included to produce analog outputs in addition to the digital output. A simplified block diagram of the model 805 is shown in Figure 3.6.

The signal and trigger inputs of model 805 are connected to the signal and trigger outputs of the pulse spectrometer. The input and output connection block diagram is shown in Figure 3.7. The  $\bar{Z}$  out is used for retrace blanking when driving a scope in the X-Y mode as a trigger signal for use with a scope in the triggered mode. Y out produces a repetitive analog reconstruction of the memory contents.

### 3.2.3 DC Magnet

The Varian Associates electromagnet used in this experiment has 12" diameter pole faces. The magnet is capable of supplying a field up to  $10^4$  Gauss with an air gap of 2.5 inches. In the CW experiment the sweep

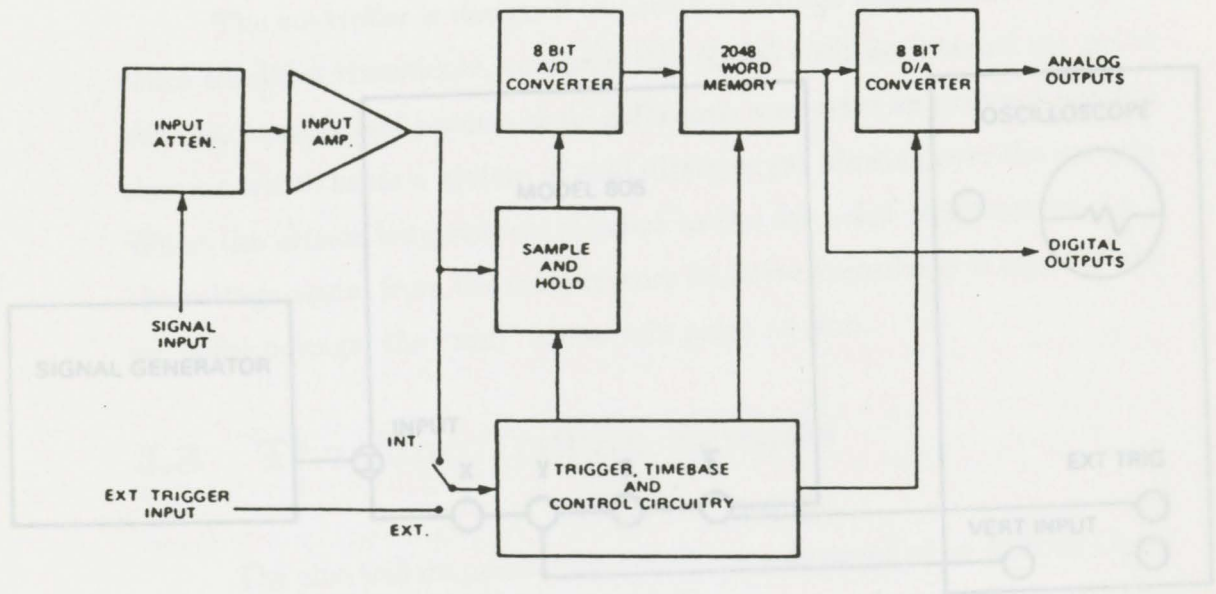


Figure 3.6: Block diagram of Model 805 Biomation Waveform Recorder

range was 25 Gauss and the sweep time was 2.5 minutes.

### 3.2.4 The Model DTC-500 Cryogenic Temperature Controller

The controller is designed to accept a voltage signal from a temperature sensitive transducer, compare this signal with an internal set point voltage, amplify and process their difference, and drive an actuator element which heats a system of cold nitrogen gas blowing over the sample. When the sensor temperature is equal to the set point temperature the voltage signal from the temperature sensitive transducer is equal to the set point voltage the "null" meter will point to zero.

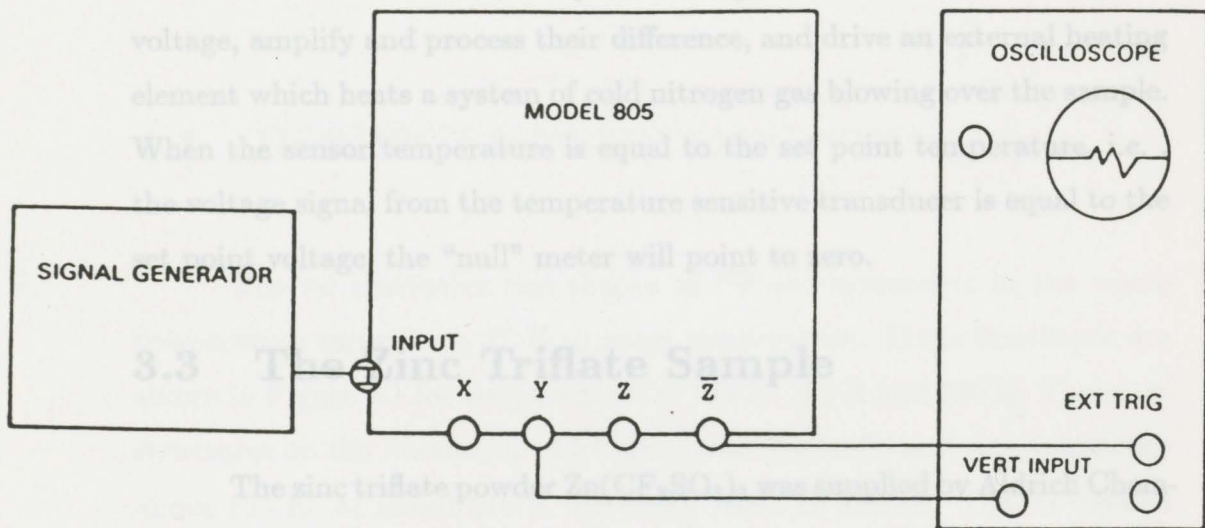


Figure 3.7: The input and output of Model 805 Biomation Waveform Recorder

The sample temperature was measured by means of a copper-constantan thermocouple and displayed on the series 400A Digital Trendicator. The accuracy was  $\pm 1K$ .

range was 25 Gauss and the sweep time was 2.5 minutes.

### 3.2.4 The Model DTC-500 Cryogenic Temperature Controller

The controller is designed to accept a voltage signal from a temperature sensitive transducer, compare this signal with an internal set point voltage, amplify and process their difference, and drive an external heating element which heats a system of cold nitrogen gas blowing over the sample. When the sensor temperature is equal to the set point temperature, i.e., the voltage signal from the temperature sensitive transducer is equal to the set point voltage, the "null" meter will point to zero.

## 3.3 The Zinc Triflate Sample

The zinc triflate powder  $\text{Zn}(\text{CF}_3\text{SO}_3)_2$  was supplied by Aldrich Chemical Company, Inc. and its purity is 98%. The zinc triflate powder is corrosive and hygroscopic so it was filled into the sample tube in a nitrogen gas bag. The sample tube was then sealed.

## 3.4 The Measurement of Temperature

The sample temperature was measured by means of a copper-constantan thermocouple and displayed on the series 400A Digital Trendicator. The accuracy was  $\pm 1\text{K}$ .

## Chapter 4

# Results and Discussion

### 4.1 Results

The cw derivative line shapes of  $^{19}\text{F}$  are symmetric in the whole temperature range from 77 K to room temperature. Three lineshapes are shown in Figure 4.1 for temperatures of 129 K, 190 K and 290 K. There are structures on the lineshape, which disappear gradually and simultaneously above 155 K. At about 210 K the width starts to narrow. The  $^{19}\text{F}$  second moment  $M_2$  over the temperature range is shown in Figure 4.2. Each experimental second moment quoted is the average value obtained from at least six experimental curves.  $M_2$  has the plateau value of  $7.17 \pm 0.13$  Gauss<sup>2</sup> up to about 136 K. It then decreases to a second plateau value of  $2.12 \pm 0.10$  Gauss<sup>2</sup> from 244 K to room temperature. These two values are the average of the second moments measured in the associated temperature ranges.

The  $T_1$  of the  $^{19}\text{F}$  of zinc triflate does not obey the exponential law, i.e., the  $\ln[(A_0 - A(\tau))/A_0]$  vs  $\tau$  is not quite a straight line (Figure 4.3). There are two or three points lying above the supposed straight line. We calculated the  $T_1$  using the linear portion of the graph near  $\tau = 0$ . The

Figure 4.1: The line shapes at 129 K (top), at 190 K (middle) and at 290 K (bottom)

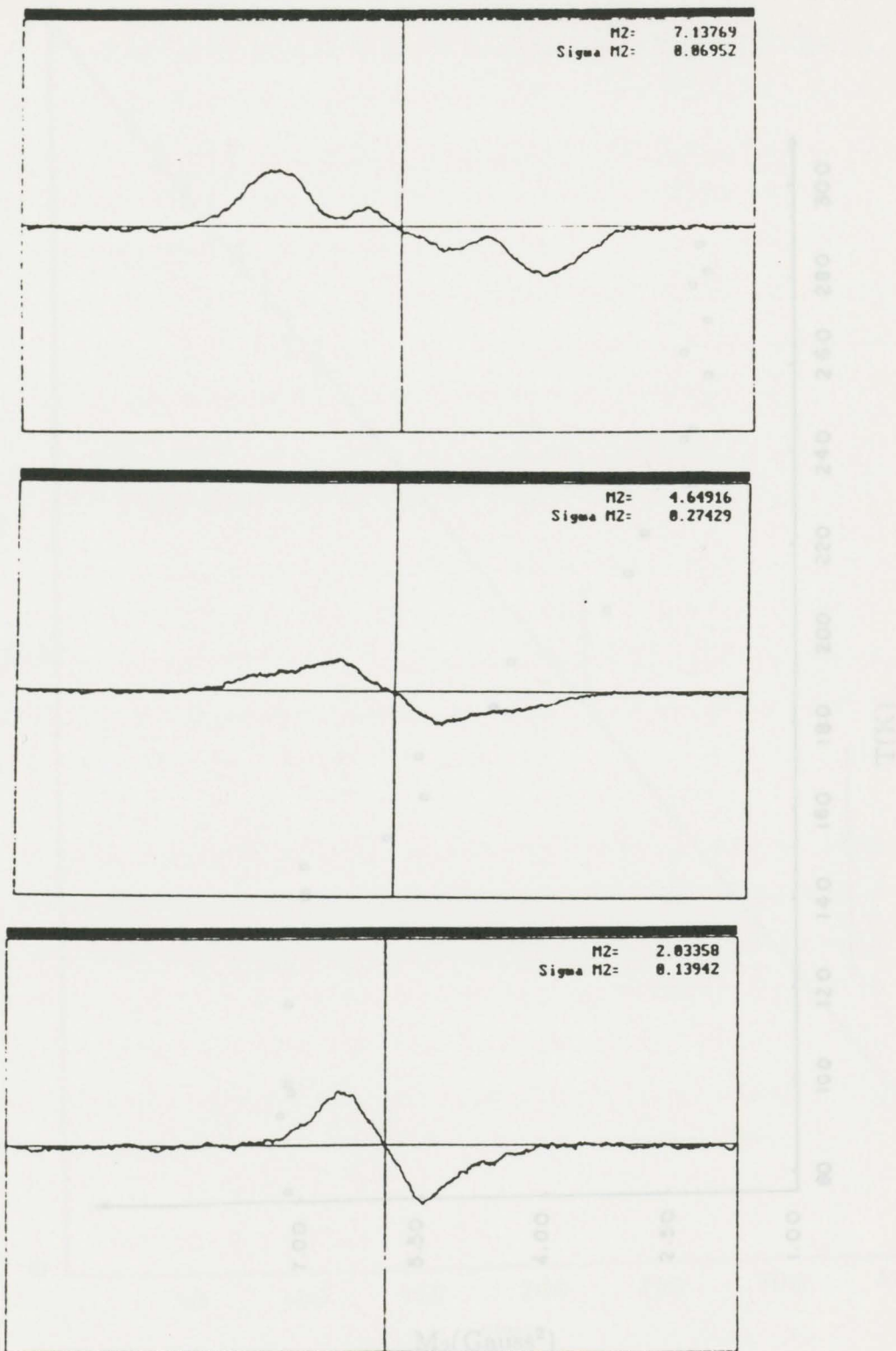


Figure 4.1: The line shapes at 129 K (top), at 190 K (middle) and at 290 K (bottom)

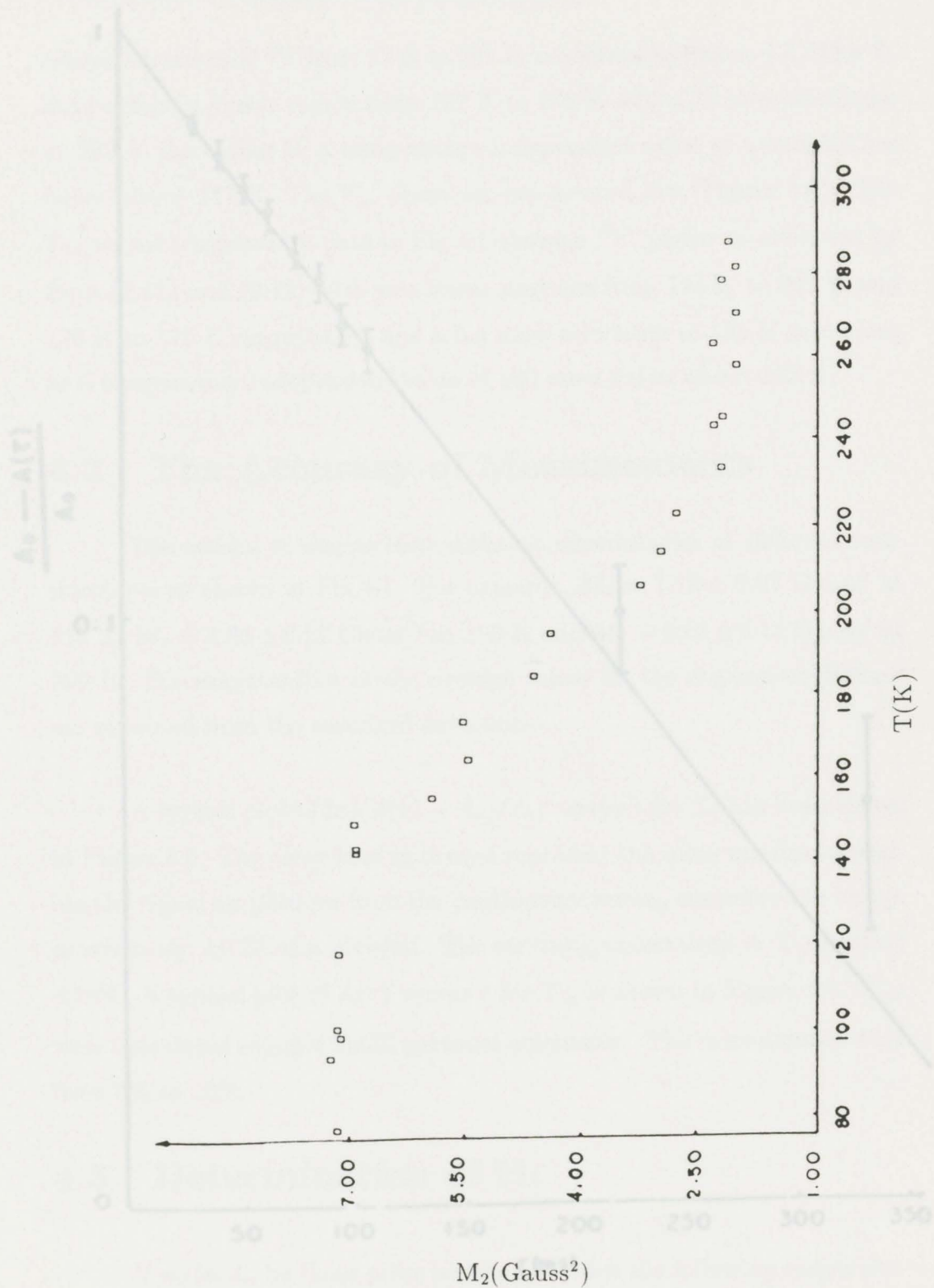


Figure 4.2: Temperature dependence of second moment at 30 MHz

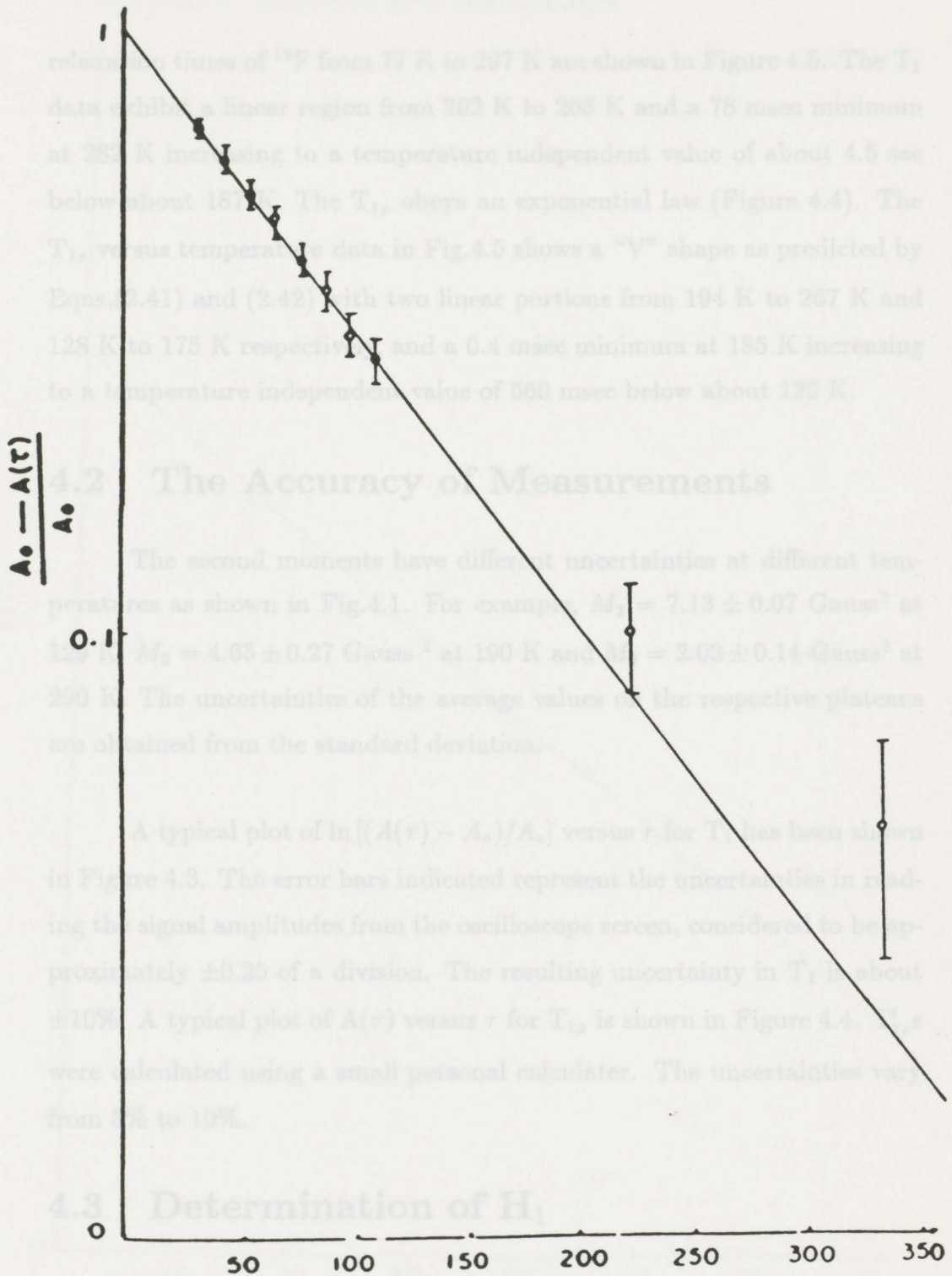


Figure 4.3: A typical plot of  $[(A_0 - A(\tau))/A_0]$  vs  $\tau$

relaxation times of  $^{19}\text{F}$  from 77 K to 297 K are shown in Figure 4.5. The  $T_1$  data exhibit a linear region from 202 K to 268 K and a 78 msec minimum at 282 K increasing to a temperature independent value of about 4.5 sec below about 187 K. The  $T_{1\rho}$  obeys an exponential law (Figure 4.4). The  $T_{1\rho}$  versus temperature data in Fig.4.5 shows a "V" shape as predicted by Eqns.(2.41) and (2.42) with two linear portions from 194 K to 267 K and 128 K to 175 K respectively, and a 0.4 msec minimum at 185 K increasing to a temperature independent value of 560 msec below about 123 K.

## 4.2 The Accuracy of Measurements

The second moments have different uncertainties at different temperatures as shown in Fig.4.1. For example,  $M_2 = 7.13 \pm 0.07$  Gauss<sup>2</sup> at 129 K,  $M_2 = 4.65 \pm 0.27$  Gauss<sup>2</sup> at 190 K and  $M_2 = 2.03 \pm 0.14$  Gauss<sup>2</sup> at 290 K. The uncertainties of the average values on the respective plateaus are obtained from the standard deviation.

A typical plot of  $\ln[(A(\tau) - A_0)/A_0]$  versus  $\tau$  for  $T_1$  has been shown in Figure 4.3. The error bars indicated represent the uncertainties in reading the signal amplitudes from the oscilloscope screen, considered to be approximately  $\pm 0.25$  of a division. The resulting uncertainty in  $T_1$  is about  $\pm 10\%$ . A typical plot of  $A(\tau)$  versus  $\tau$  for  $T_{1\rho}$  is shown in Figure 4.4.  $T'_{1\rho}$ s were calculated using a small personal calculator. The uncertainties vary from 5% to 10%.

## 4.3 Determination of $H_1$

If we let  $t_w$  be those pulse widths for which the following magnetiza-

Figure 4.4: A typical  $T_{1\rho}$  calculation graph.

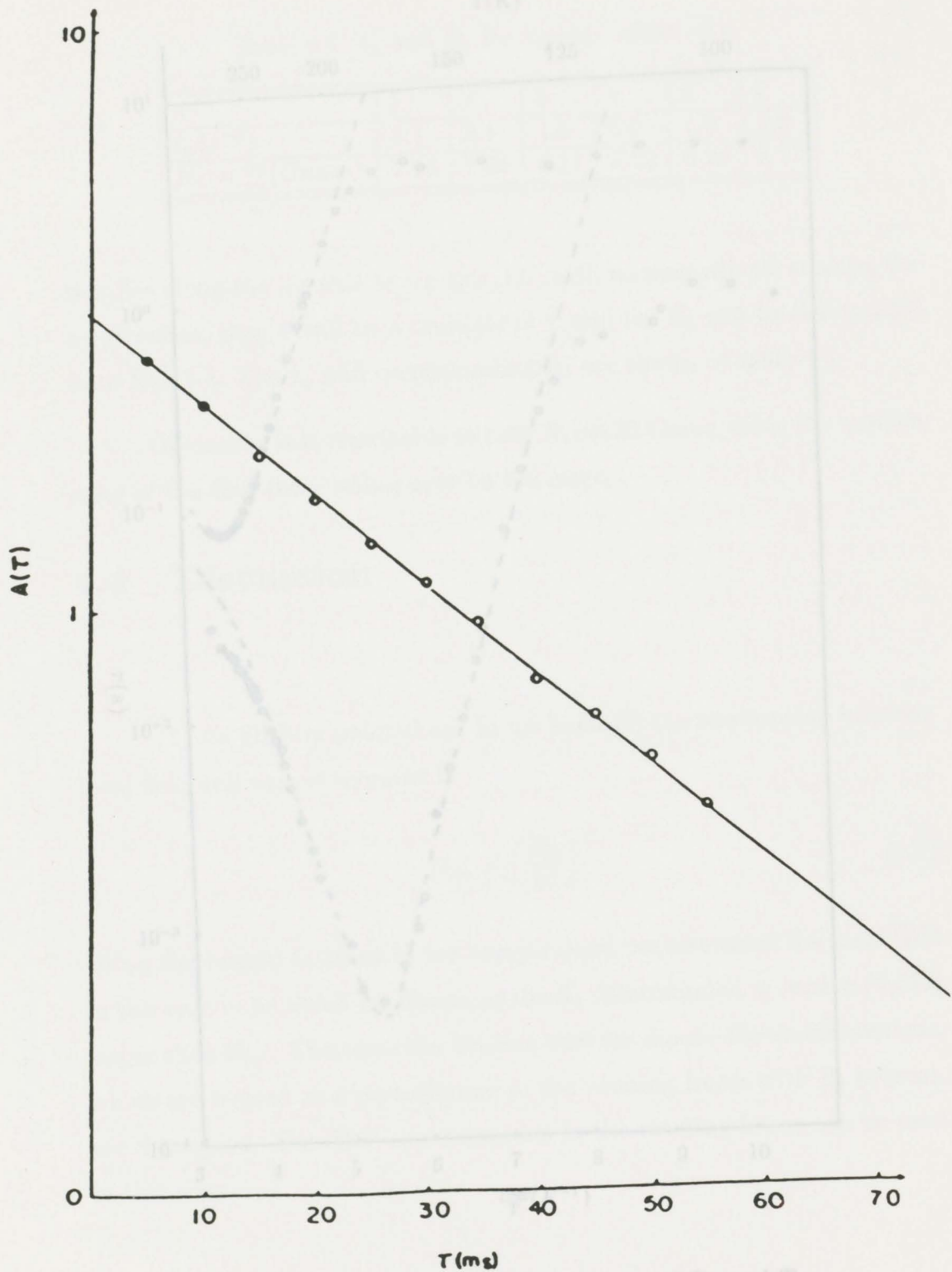


Figure 4.5: Temperature dependence of  $T_1$  and  $T_{1p}$ .

Figure 4.4: A typical  $T_{1p}$  calculation graph.

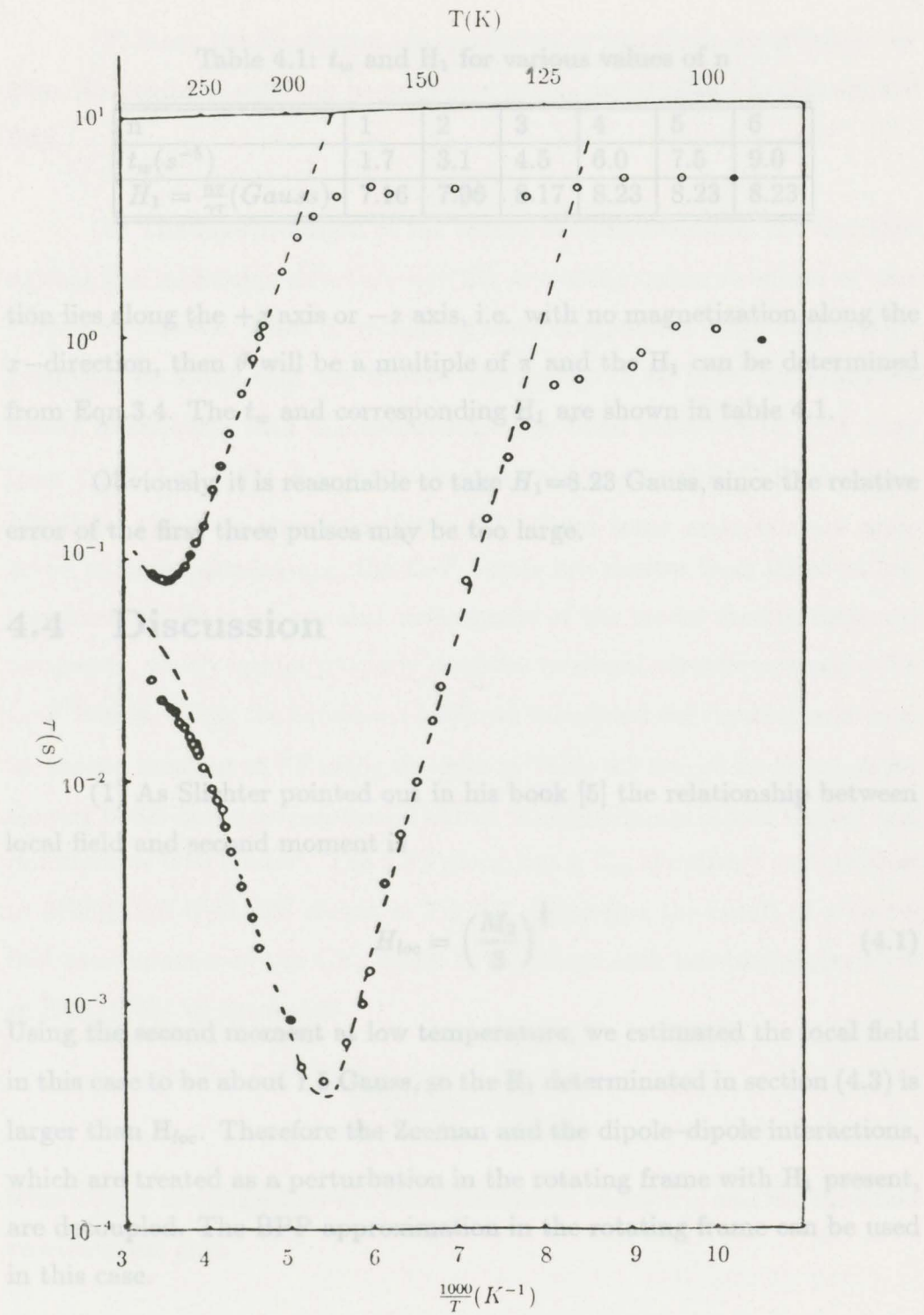


Figure 4.5: Temperature dependence of  $T_1$  and  $T_{1\rho}$

Table 4.1:  $t_w$  and  $H_1$  for various values of  $n$ 

$n$	1	2	3	4	5	6
$t_w(s^{-5})$	1.7	3.1	4.5	6.0	7.5	9.0
$H_1 = \frac{n\pi}{\gamma\tau}(\text{Gauss})$	7.16	7.96	8.17	8.23	8.23	8.23

tion lies along the  $+z$  axis or  $-z$  axis, i.e. with no magnetization along the  $x$ -direction, then  $\theta$  will be a multiple of  $\pi$  and the  $H_1$  can be determined from Eqn.3.4. The  $t_w$  and corresponding  $H_1$  are shown in table 4.1.

Obviously, it is reasonable to take  $H_1=8.23$  Gauss, since the relative error of the first three pulses may be too large.

## 4.4 Discussion

(1) As Slichter pointed out in his book [5] the relationship between local field and second moment is

$$H_{loc} = \left(\frac{M_2}{3}\right)^{\frac{1}{2}} \quad (4.1)$$

Using the second moment at low temperature, we estimated the local field in this case to be about 1.5 Gauss, so the  $H_1$  determined in section (4.3) is larger than  $H_{loc}$ . Therefore the Zeeman and the dipole-dipole interactions, which are treated as a perturbation in the rotating frame with  $H_1$  present, are decoupled. The BPP approximation in the rotating frame can be used in this case.

(2) Since the lineshapes are symmetric in the whole temperature region, the chemical shift can be neglected in this material and in this applied field.

(3) The interpretation of the results is complicated by the fact that neither the molecular structure nor the crystallographic structure of zinc triflate are known. After investigating some compounds containing triflate group(s), we found that the triflate  $\text{CF}_3$  groups in all these materials are nearly tetrahedral with  $C_{3v}$  symmetry. The bond distances of C–F vary from 1.302 Å to 1.334 Å and the average bond angles of F–C–F vary from 108.5° to 110.5° as shown in Table 4.2. Since some materials are measured at high temperature, the C–F bonds are shorter than those at low temperature. This is a natural consequence of the model used in those experiments, which cannot properly describe torsional vibrations around the C–F bonds. Using the equation (2.29), we calculated the rigid intramolecular second moment of  $^{19}\text{F}$  using the data in Table 4.2 except for those rather shorter bond distances mentioned above. The maximum is 6.84 Gauss<sup>2</sup> and minimum is 6.10 Gauss<sup>2</sup>. The  $\text{CF}_3$  group has a  $C_{3v}$  symmetry such as that in  $2\text{CF}_3\text{SO}_3\text{H}\cdot\text{H}_2\text{O}$  [28] shown in Fig.4.6. Therefore the result of a threefold reorientation of the  $\text{CF}_3$  group is to reduce each intramolecular term in Eqn.(2.29) by the factor

$$\frac{(3 \cos^2 \gamma_{jk} - 1)^2}{4}$$

where  $\gamma_{jk}$  is the angle between the internuclear vector  $\mathbf{r}_{jk}$  and the threefold reorientation axis.

Since  $\gamma_{jk} = 90^\circ$  for all the intramolecular interfluorine vectors in threefold rotation, the reduction factor is 1/4. The threefold reorientation

Table 4.2: The parameters of  $CF_3$  groups in different compounds.

compounds	bond length of C-F	bond angle of F-C-F
$2CF_3SO_3H \cdot H_2O$ [28]	C-F(1) 1.327Å	F(1)-C-F(2) 108.7°
	C-F(2) 1.314Å	F(1)-C-F(3) 109.0°
	C-F(3) 1.315Å	F(2)-C-F(3) 109.7°
$H_3O^+CF_3SO_3^-$ [29]	C-F(1) 1.299Å	F(1)-C-F(2) 107.8°
	C-F(2) 1.319Å	F(1)-C-F(3) 108.1°
	C-F(3) 1.321Å	F(2)-C-F(3) 109.3°
$H_3O^+CF_3SO_3^-$ [30]	C-F(1) 1.307Å	F(1)-C-F(2) 108.4°
	C-F(2) 1.316Å	F(1)-C-F(3) 108.2°
	C-F(3) 1.302Å	F(2)-C-F(3) 109.6° <sup>a</sup>
	C-F(1) 1.332Å	F(1)-C-F(2) 109.5°
	C-F(2) 1.332Å	F(1)-C-F(3) 108.9°
	C-F(3) 1.334Å	F(2)-C-F(3) 108.4° <sup>b</sup>
$H_9O_4^+CF_3SO_3^-$ [31]	C-F(1) 1.324Å	F(1)-C-F(2) 108.3°
	C-F(2) 1.328Å	F(1)-C-F(3) 108.8°
	C-F(3) 1.333Å	F(2)-C-F(3) 108.4°
$H_5O_2^+CF_3SO_3^-$ [32]	C-F(1) 1.316Å	F(1)-C-F(2) 107.8°
	C-F(2) 1.308Å	F(1)-C-F(3) 108.1°
	C-F(3) 1.316Å	F(2)-C-F(3) 109.7° <sup>c</sup>
	C-F(1) 1.327Å	F(1)-C-F(2) 108.7°
	C-F(2) 1.322Å	F(1)-C-F(3) 109.9°
	C-F(3) 1.318Å	F(2)-C-F(3) 109.9° <sup>d</sup>
$H_3O^+CF_3SO_3^- \cdot 4H_2O$ [33]	C-F(1) 1.328Å	F(1)-C-F(2) 108.0°
	C-F(2) 1.330Å	F(1)-C-F(3) 108.8°
	C-F(3) 1.329Å	F(2)-C-F(3) 108.1°
$[Nd^{3+}(H_2O)_9](CF_3SO_3)_3$ [34]	C-F(1) 1.311Å	F(1)-C-F(2) 109.3°
	C-F(2) 1.301Å	F(1)-C-F(3) 109.4°
$[Ho^{3+}(H_2O)_9](CF_3SO_3)_3$ [34]	C-F(1) 1.330Å	F(1)-C-F(2) 110.4°
	C-F(2) 1.296Å	F(1)-C-F(3) 110.5°

<sup>a</sup>measured at 296 K<sup>b</sup>measured at 83 K<sup>c</sup>measured at 225 K<sup>d</sup>measured at 85 K

Since  $\gamma_{jk} = 90^\circ$  for all the intramolecular interfluorine vectors in threefold rotation, the reduction factor is 1/4. The threefold reorientation

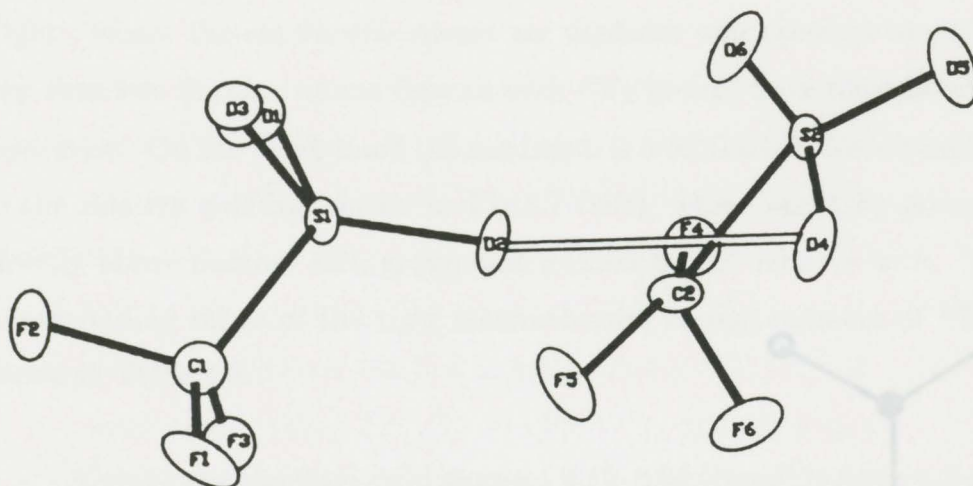


Figure 4.6:  $\text{CF}_3$  is tetrahedral with  $\text{C}_{3v}$  symmetry in  $2\text{CF}_3\text{SO}_3\text{H}\cdot\text{H}_2\text{O}$

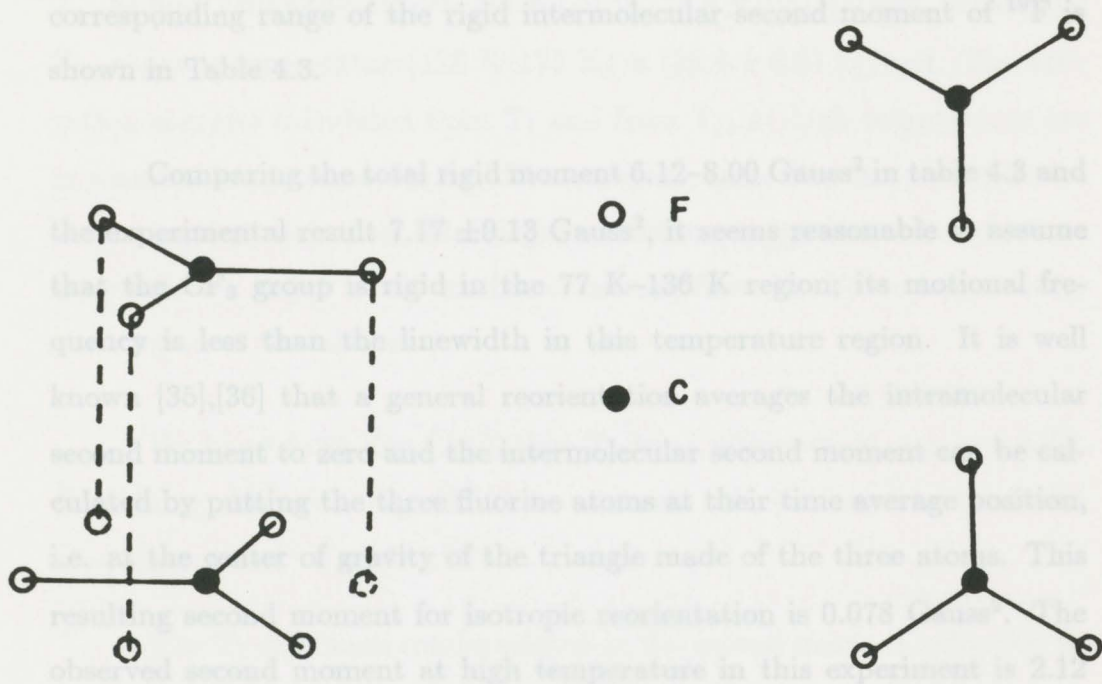
Table 4.3: The second moment of  $^{19}\text{F}$  in motion

motion	intra( $\text{Gauss}^2$ )	inter( $\text{Gauss}^2$ )	total( $\text{Gauss}^2$ )
rigid	6.10–6.84	0.02–1.16	6.12–8.00
threefold	1.52–1.71	0.078	1.60–1.79

result is shown in the Table 4.3.

Using the crystal structures of the materials listed in Table 4.2, we calculated the distance between the nearest carbon pair. The shortest one is  $4.8027 \text{ \AA}$  in  $2\text{CF}_3\text{SO}_3\text{H}\cdot\text{H}_2\text{O}$  [28]. Since the second moment is proportional to  $r^{-6}$ , the intermolecular contribution to the F–F second moment will be much smaller for larger F–F distances. Taking into account the different possible relative positions of the two  $\text{CF}_3$  groups in  $2\text{CF}_3\text{SO}_3\text{H}\cdot\text{H}_2\text{O}$ , we found the maximum intermolecular second moment of  $^{19}\text{F}$  is  $1.16 \text{ Gauss}^2$

corresponding to the relative position of  $\text{CF}_3$  groups shown in Figure 4.7 (right), where the six fluorine atoms are coplanar and oriented in such a way that two fluorine atoms (one in each  $\text{CF}_3$  group) have their shortest separation. On the other hand the minimum is  $0.02 \text{ Gauss}^2$ , corresponding to the relative position shown in Fig.4.7 (left), where one  $\text{CF}_3$  group is directly above another  $\text{CF}_3$  group and rotated by  $60^\circ$  relative to it. The corresponding range of the rigid intermolecular second moment of  $^{19}\text{F}$  shown in Table 4.3.



Comparing the total rigid moment  $6.12-8.00 \text{ Gauss}^2$  in table 4.3 and the experimental result  $7.17 \pm 0.13 \text{ Gauss}^2$ , it seems reasonable to assume that the  $\text{CF}_3$  group is rigid in the  $77 \text{ K}-136 \text{ K}$  region; its motional frequency is less than the linewidth in this temperature region. It is well known [35],[36] that a general reorientation averages the intramolecular second moment to zero and the intermolecular second moment can be calculated by putting the three fluorine atoms at their time average position, i.e. at the center of gravity of the triangle made of the three atoms. This resulting second moment for isotropic reorientation is  $0.078 \text{ Gauss}^2$ . The observed second moment at high temperature in this experiment is  $2.12 \text{ Gauss}^2$ , so we can rule out a general isotropic reorientation even at high temperature and propose that at higher temperature the threefold reorientational motion of the  $\text{CF}_3$  group predominates since the second moment at higher temperature is about the sum of the threefold intramolecular second moment and the residual intermolecular second moment.

Figure 4.7: The two extreme relative positions of two  $\text{CF}_3$  groups

the reorientation rate of the  $\text{CF}_3$  group in the  $\text{CF}_3$  group of a trisulfate is nonexponential is reasonable, since it results from a dipole-dipole nuclear interaction of a three spin system [37], [38].  $A(\tau)$  should be a sum

corresponding to the relative position of  $\text{CF}_3$  groups shown in Figure 4.7 (right), where the six fluorine atoms are coplanar and oriented in such a way that two fluorine atoms (one in each  $\text{CF}_3$  group) have their shortest separation. On the other hand the minimum is  $0.02 \text{ Gauss}^2$ , corresponding to the relative position shown in Fig.4.7 (left), where one  $\text{CF}_3$  group is directly above another  $\text{CF}_3$  group and rotated by  $60^\circ$  relative to it. The corresponding range of the rigid intermolecular second moment of  $^{19}\text{F}$  is shown in Table 4.3.

Comparing the total rigid moment  $6.12\text{--}8.00 \text{ Gauss}^2$  in table 4.3 and the experimental result  $7.17 \pm 0.13 \text{ Gauss}^2$ , it seems reasonable to assume that the  $\text{CF}_3$  group is rigid in the  $77 \text{ K--}136 \text{ K}$  region; its motional frequency is less than the linewidth in this temperature region. It is well known [35],[36] that a general reorientation averages the intramolecular second moment to zero and the intermolecular second moment can be calculated by putting the three fluorine atoms at their time average position, i.e. at the center of gravity of the triangle made of the three atoms. This resulting second moment for isotropic reorientation is  $0.078 \text{ Gauss}^2$ . The observed second moment at high temperature in this experiment is  $2.12 \text{ Gauss}^2$ , so we can rule out a general isotropic reorientation even at high temperature and propose that at higher temperature the threefold reorientational motion of the  $\text{CF}_3$  group predominates since the second moment at higher temperature is about the sum of the threefold intramolecular second moment and the residual intermolecular second moment.

(4) That the relaxation time of fluorine in the  $\text{CF}_3$  group of zinc triflate is nonexponential is reasonable, since it results from a dipole-dipole nuclear interaction of a three spin system [37], [38].  $A(\tau)$  should be a sum

of exponentials but in this case the different relaxation times were too close to be identified and extracted separately. We calculated the slope using the initial linear part near  $\tau = 0$ , which is still a good approximation of the BPP theory. From Fig 4.5, we extract the activation energy  $E_a$  from the slopes of the linear portions of the curves. The activation energy  $E_a$  calculated from  $T_1$  in the temperature region 202 K–268 K, is  $(21.9 \pm 0.5)$  kJ/mol; from  $T_{1\rho}$  at high temperature (194–267 K), it is  $(23.9 \pm 0.5)$  kJ/mol, while from  $T_{1\rho}$  at lower temperature (128 K–175 K) is  $(28.4 \pm 0.6)$  kJ/mol. The activation energies calculated from  $T_1$  and from  $T_{1\rho}$  at high temperature are in reasonable agreement as could be expected, since they are nearly in the same temperature region. The larger activation energy at low temperature may reflect a larger steric hindrance arising from the lower temperature contraction of the lattice.

We know from Eqn.(2.40) that  $T_1$  has a minimum at  $\omega_o\tau_c = 0.6158$ . Combining this with Eqn.(2.42) we estimate the pre-exponential factor  $\tau_o = (2.83 \pm 0.67) \times 10^{-13}$  s.

The  $T_1$  minimum can be related to the second moment reduction by

$$\Delta M_2 = \frac{1.05\omega_o}{\gamma^2 T_1(\min)} = 4.1 \text{ Gauss}^2$$

As mentioned in section 4.2, the uncertainty of the  $T_1$  measurement is  $\pm 10\%$ , so  $\Delta M_2 = 4.1 \pm 0.4 \text{ Gauss}^2$ . Comparing it with the observed second moment reduction  $5.05 \pm 0.23 \text{ Gauss}^2$  and the theoretical second moment  $4.33\text{--}6.40 \text{ Gauss}^2$ , we can say they agree well and conclude that the  $M_2$  reduction and  $T_1$  minimum arise from the same mechanism, namely the threefold reorientation of the  $\text{CF}_3$  group.

From Eqn.(2.41), we know that  $T_{1\rho}$  has a minimum at  $\omega_1\tau_c = 0.5$ . Combining (2.41) and (2.42) we can estimate the temperature at which the  $T_{1\rho}$  minimum should occur for the  $T_1$  rotation mechanism. The result is 177 K, which is quite close to the temperature at which the  $T_{1\rho}$  minimum is observed to occur (185 K), and we conclude that the  $T_{1\rho}$  minimum also arises from the same mechanism. The discrepancy may be due to the change of  $E_a$  with temperature. Combining the values  $\omega_1\tau_c = 0.5$  and  $T_{1\rho}$  with the activation energy  $E_a = 28.4$  kJ/mol we estimated the pre-exponential factor  $\tau_o = (2.38 \pm 1.13) \times 10^{-14}$  s at low temperature, while combining  $E_a = 23.9$  kJ/mol we estimated the  $\tau_o = (3.96 \pm 1.60) \times 10^{-13}$  s at high temperature (Table 4.4). Putting the parameters  $\Delta M_2$ ,  $\tau_o$  and  $E_a$  in different temperature regions into Eqn.(2.40), (2.41) and (2.42), we get two curves of  $T_1$  vs  $\frac{1}{T}$  and  $T_{1\rho}$  vs  $\frac{1}{T}$ . These are shown as the dashed curves in Figure 4.5 and agree very well with the  $T_1$  and  $T_{1\rho}$  data down to 187 K and 123 K respectively, below which temperatures the relaxation times are much shorter and considerably less temperature sensitive than the BPP theory would predict. An explanation of such shortened values of  $T_1$  and  $T_{1\rho}$  is given by the theory of paramagnetic impurities put forward by Rollin and Hatton [39], Darby and Rollin [40], and by Bloembergen[41]. According to the theory, the electron relaxation and the spin diffusion can be the dominant relaxation mechanisms at low temperature with an impurity concentration of as little as one part in  $10^6$ .

## 4.5 Summary

In this thesis a study of the reorientation of tetrahedral  $CF_3$  ions in solid zinc triflate by NMR has been described. The results are summarized

Table 4.4: The pre-exponential factors  $\tau_0$  and activation energy  $E_a$ 

extract from	temperature region	$\tau_0$	$E_a$
$T_1$	202 K–268 K	$2.83 \times 10^{-13}$ s	21.9 kJ/mol
$T_{1\rho}$	194 K–267 K	$3.96 \times 10^{-13}$ s	23.9 kJ/mol
$T_{1\rho}$	128 K–175 K	$2.38 \times 10^{-14}$ s	28.4 kJ/mol

below:

(1) The decays of the magnetization of  $^{19}\text{F}$  in zinc triflate along the external magnetic field  $H_0$  in the laboratory frame do not obey the exponential law while the decay along  $H_1$  in the rotating frame does obey the exponential law.

(2) The curves of  $T_1$  vs temperature and  $T_{1\rho}$  vs temperature show a “V” shape as expected. The leveling off of  $T_1$  and  $T_{1\rho}$  with decreasing temperature is probably the result of relaxation by paramagnetic impurities. The agreement between the theoretical and experimental  $T_1$  and  $T_{1\rho}$  data above 187 K and 123 K respectively, is a good indication that the theory we are applying in this thesis is correct.

the pre-exponential factor  $\tau_0$  is  $2.83 \times 10^{-13}$  s and the activation energy is about 23 kJ/mol while in the low temperature region below 185 K,  $\tau_0$  is  $1.38 \times 10^{-14}$  s and  $E_a$  is 28 kJ/mol. These values are comparable with those in other molecular solids [14]. The increase in activation energy at low temperature may be due to a larger steric hindrance arising from the lower temperature contraction of the lattice.

(4) The lineshape of  $^{19}\text{F}$  begins to narrow at about 210 K. The chemical shift in this case could be neglected. Since the crystal structure of zinc

triflate is unknown, no attempt has been made to fit the lineshape and interpret low temperature structural features.

(5) In the region 77 K  $\sim$  136 K the lattice of the  $\text{CF}_3$  group is essentially rigid (any rotational frequency is less than the linewidth), while the threefold reorientation of  $\text{CF}_3$  predominates above 185 K.

(6) The theoretical reduction of second moment of  $^{19}\text{F}$  in zinc triflate of 4.33–6.40 Gauss<sup>2</sup> is in reasonable agreement with the observed experimental reduction of  $5.05 \pm 0.23$  Gauss<sup>2</sup> and the second moment reduction from  $T_1(\text{min})$  of  $4.1 \pm 0.4$  Gauss<sup>2</sup>. The temperature of 185 K at which the  $T_{1\rho}$  minimum occurs is quite close to 177 K, the estimated value from BPP theory. The dashed lines in Fig.4.5, derived from the BPP theory, agree very well with the observed data except at low temperatures. The agreement between the theory and experiment indicate that the BPP theory is valid in this case and that the same motional mechanism ( $\text{CF}_3$  rotation) is responsible for the relaxation in the laboratory and rotating frames, and the second moment reduction.

## 4.6 Suggestions

It may be useful to extend this work as follows:

(1) The same kind of investigation, i. e., the measurements of second moment, relaxation time in the laboratory and relaxation time in the rotating frame, from room temperature down to 77 K, in similar materials containing the triflate group ( $\text{CF}_3\text{SO}_3$ ), such as lithium triflate ( $\text{LiCF}_3\text{SO}_3$ ), may help to confirm the results found in this type of molecule.

## References

(2) If the crystal structure of zinc triflate could be determined, some uncertainties in this experiment may be decreased or eliminated.

(3) Since the chemical shift is dependent on the field, it may be useful to measure the absorption line at higher  $H_0$  fields, which might be done next year when the new equipment currently under development for the lab is available.

- [2] F. Bloch, W. W. Hansen and M. Packard, Phys. Rev., **70**, 474 (1946)
- [3] A. Abragam, The Principles of Nuclear Magnetism, Oxford University Press (1961)
- [4] E. R. Andrew, Nuclear Magnetic Resonance, Cambridge (1958)
- [5] C. F. Slichter, Principles of Magnetic Resonance, Springer-Verlag, Berlin (1978)
- [6] C. J. Gorter, Physica, **3**, 995 (1936)
- [7] C. J. Gorter, and L. J. F. Broer, Physica, **9**, 591 (1942)
- [8] C. J. Gorter, Physica, **17**, 169 (1951)
- [9] E. L. Hahn, Phys. Rev., **80**, 580 (1950)
- [10] H. S. Gutowsky, G. B. Kistiakowsky, G. E. Pake and E. M. Purcell, J. Chem. Phys., **17**, 972 (1949)
- [11] H. S. Gutowsky and G. E. Pake, J. Chem. Phys., **18**, 162 (1950)
- [12] E. M. Purcell, Physica, **17**, 232 (1950)

# References

- [1] E. M. Purcell, H. C. Torrey and R. V. Pound, Phys. Rev., **69**, 37 (1946)
- [2] F. Bloch, W. W. Hansen and M. Packard, Phys. Rev., **70**, 474 (1946)
- [3] A. Abragam, The Principles of Nuclear Magnetism, Oxford University Press (1961)
- [4] E. R. Andrew, Nuclear Magnetic Resonance, Cambridge (1958)
- [5] C. P. Slichter, Principles of Magnetic Resonance, Springer-Verlag, Berlin (1978)
- [6] C. J. Gorter, Physica, **3**, 995 (1936)
- [7] C. J. Gorter, and L. J. F. Broer, Physica, **9**, 591 (1942)
- [8] C. J. Gorter, Physica, **17**, 169 (1951)
- [9] E. L. Hahn, Phys. Rev., **80**, 580 (1950)
- [10] H. S. Gutowsky, G. B. Kistiakowsky, G. E. Pake and E. M. Purcell, J. Chem. Phys., **17**, 972 (1949)
- [11] H. S. Gutowsky and G. E. Pake, J. Chem. Phys., **18**, 162 (1950)
- [12] E. M. Purcell, Physica, **17**, 282 (1950)

- and Bolts Approach, Addison-Wesley Publishing Company, Inc. (1981)
- [13] M. R. Barr and B. A. Dunell, Canad. J. Chem., **48**, 895 (1970)
- [14] G. E. Kibrik, I. A. Kyuntsel', V. A. Mokeeva, Yu. I. Rozenberg and G. B. Soifer, Sov. Phys. Solid Stste, **17**, 598 (1975)
- [15] S. Miyajima, N. Nakamura and H. Chihara, J. Phys. Soc. Japan, **49**, 1867 (1980)
- [16] A. Watton, E. Koster, H. S. Sandhu and H. E. Petch, J. Chem. Phys., **70**, 5197 (1978)
- [17] A. Watton, E. Koster and H. E. Petch, J. Chem. Phys., **74**, 2755 (1981)
- [18] A. Watton, J. C. Pratt, E. C. Reynhardt and H. E. Petch, J. Chem. Phys., **77**, 2344 (1982)
- [19] F. Bloch Phys. Rev., **70**, 460 (1946)
- [20] J. H. Van Vleck, Phys. Rev., **74**, 1168 (1948)
- [21] N. Bloembergen, E. M. Purcell and R. V. Pound, Phys. Rev., **73**, 679 (1948)
- [22] G. P. Jones, Phys. Rev., **148**, 332 (1966)
- [23] R. Kub and K. Tomita, J. Phys. Soc. Japan, **9**, 888 (1954)
- [24] D. C. Look and I. J. Lowe, J. Chem. Phys., **44**, 2995 (1966)
- [25] E. Fukushima and S. B. W. Roeder, Experimental Pulse NMR, A Nuts

and Bolts Approach, Addison-Wesley Publishing Company, Inc. (1981)

- [26] E. R. Andrew, Phys. Rev., **91**, 425(1953)
- [27] G. V. H. Wilson, J. Sci. Instrum., **41**, 98 (1964)
- [28] R. G. Delaplane, J-O Lundgren, and I. Olovsson, Acta Cryst., **B31**, 2208 (1975)
- [29] J-O Lundgren, R. Tellgren and I. Olovsson, Acta Cryst., **B34**, 2945 (1978)
- [30] J. B. Spencer and J-O Lundgren, Acta Cryst., **B29**, 1923 (1973)
- [31] J-O Lundgren, Acta Cryst., **B34**, 2428 (1978)
- [32] R. G. Delaplane, J-O Lundgren and I. Olovsson, Acta Cryst., **B31**, 2202 (1975)
- [33] J-O Lundgren, Acta Cryst., **B34**, 2432 (1978)
- [34] C. O. Paiva, E. E. Castellano, L. C. Machado and G. Vicetini, Inorganica Chimica Acta, **110**, 83 (1985)
- [35] E. R. Andrew and R. G. Eades, Proc. Roy. Soc. (London) Ser., **A 216**, 398 (1953)
- [36] A. Watton, E. C. Reynhardt, and H. E. Petch, J. Chem. Phys., **65**, 4370 (1976)
- [37] R. L. Hilt, R and P. S. Hubbard, Phys. Rev., **134**, A392 (1964)

- [38] L. K. Runnels, Phys. Rev., **134**, A28 (1964)
- [39] B. V. Rollin and J. Hatton, Phys. Rev., **74**, 346 (1948)
- [40] F. J. Darby and B. V. Rollin, Nature, Lond., **164**, 66 (1949)
- [41] N. Bloembergen, Physica, **15**, 386(1949)
- [42] C. R. Bruce, Phys. Rev., **107**, 43 (1953)
- [43] Thomas C. Farrar and Edwin D. Becker, Pulse and Fourier Transform NMR, Academic Press, New York, London (1971)
- [44] C. A. Fyfe, Solid State NMR for Chemists, C. F. E. Press (1984)
- [45] M. Goldman, Spin Temperature and Nuclear Magnetic Resonance in Solids, Oxford University, New York, London (1970)
- [46] S. R. Hartmann and E. L. Hahn, Phys. Rev., **128**, 2042 (1960)
- [47] M. Mehring, High Resolution NMR Spectroscopy in Solids, New York (1976)
- [48] Yu. N. Moskvich and B. I. Cherkasov, Sov. Phys. Solid State, **21**, 161 (1979)
- [49] C. P. Jr. Poole and H. A. Farach, Relaxation in Magnetic Resonance, New York and London (1971)
- [50] F. A. Rushworth and D. P. Tunstall, Nuclear Magnetic Resonance, New York (1973)
- [51] A. K. Saha, and T. P. Das, Theory and Applications of Nuclear

Induction, Calcutta (1957)

[52] R. T. Scumacher, Magnetic Resonance, Principles and Application, New York (1970)

[53] A. Zalkin, J. D. Forrester and S. D. H. Templeton, Acta Cryst., **B34**, 2428 (1978)

[54] L. A. Zemnukhova, R. L. Daridovich, P. S. Gordoienco, J. Grigas, A. N. Kovrianov, S. I. Kuznetstov, T. A. Kaidalova and V. Urbonavičius, Phys. Stat. Sol., **A80**, 553 (1983)

Title of Thesis

<sup>19</sup>F NMR INVESTIGATION OF CF<sub>3</sub> MOTION  
IN SOLID ZINC TRIFLUOROMETHYLSULFONATE

Franko Šon  
Author

December 1987

VITA

## PARTIAL COPYRIGHT LICENSE

Surname: Sun

Given Name: Jiancong

Place of Birth: Shanghai, P. R. China

I hereby grant the right to lend my thesis (the title of which is shown below) to users of the University of Victoria Library, and to make single copy only for such users or in response to a request from the Library of any other university, or similar institution, on its behalf or for one of its users. I further agree that permission for extensive copying of this thesis for scholarly purposes may be granted by me or a member of the University designated by me. It is understood that copying or publication of this thesis for financial gain shall not be allowed without written permission.

Title of Thesis: *Ph.D. Thesis, Etc. , Awarded, with Dates and Names of Institutions:*

B. Sc. 1983 East China Normal University

### **<sup>19</sup>F NMR INVESTIGATION OF CF<sub>3</sub> MOTION IN SOLID ZINC TRIFLUOROMETHYLSULFONATE**

Honors and Awards:

University of Victoria Fellowship 1985-1987



Author

Publications:

---

December 1987

